J. Fluid Mech. (2013), *vol.* 720, *pp.* 104–139.
doi:10.1017/jfm.2012.640

The internal gravity wave field emitted by a stably stratified turbulent wake

Ammar M. Abdilghanie[1] **and Peter J. Diamessis**[2,†]

[1]Leadership Computing Facility, Argonne National Laboratory, Argonne, IL 60439, USA

[2]School of Civil and Environmental Engineering, Cornell University, Ithaca, NY 14853, USA

(Received 7 February 2012; revised 24 October 2012; accepted 19 December 2012;
first published online 27 February 2013)

The internal gravity wave (IGW) field emitted by a stably stratified, initially turbulent, wake of a towed sphere in a linearly stratified fluid is studied using fully nonlinear numerical simulations. A wide range of Reynolds numbers, $Re = UD/\nu \in [5 \times 10^3, 10^5]$ and internal Froude numbers, $Fr = 2U/(ND) \in [4, 16, 64]$ (U, D are characteristic body velocity and length scales, and N is the buoyancy frequency) is examined. At the higher Re examined, secondary Kelvin–Helmholtz instabilities and the resulting turbulent events, directly linked to a prolonged non-equilibrium (NEQ) regime in wake evolution, are responsible for IGW emission that persists up to $Nt \approx 100$. In contrast, IGW emission at the lower Re investigated does not continue beyond $Nt \approx 50$ for the three Fr values considered. The horizontal wavelengths of the most energetic IGWs, obtained by continuous wavelet transforms, increase with Fr and appear to be smaller at the higher Re, especially at late times. The initial value of these wavelengths is set by the wake height at the beginning of the NEQ regime. At the lower Re, consistent with a recently proposed model, the waves propagate over a narrow range of angles that minimize viscous decay along their path. At the higher Re, wave motion is much less affected by viscosity, at least initially, and early-time wave propagation angles extend over a broader range of values which are linked to increased efficiency in momentum extraction from the turbulent wake source.

Key words: stratified flows, wakes/jets, waves/free-surface flows

1. Introduction

The emission of internal gravity waves (IGWs) by submerged stably stratified turbulence is a phenomenon of relevance to environmental/naval applications and fundamental stratified flow physics. The emitted waves can drive considerable energy redistribution within the water column (Thorpe 2005), are likely to amplify and break causing mixing far from the turbulent source (Keeler, Bondur & Gibson 2005) and can serve as an energy sink additional to viscous dissipation and diapycnal mixing within the turbulent source (Riley & Metcalfe 1987; Spedding 2002). A broad body of literature dedicated to the study of IGW emission by stratified turbulence has revealed a phenomenon with extremely complex underlying physics. This complexity is compounded by the strong dependence of IGW and turbulence properties on the governing parameters, the degree of spatial localization of the source

† Email address for correspondence: pjd38@cornell.edu

and whether the turbulent source is as stably stratified as the ambient fluid or is well-mixed.

1.1. *IGW radiation from turbulent mixed regions*

We first review work on the radiation of IGWs from a well-mixed, continually forced, turbulent source into an overlying/underlying stably stratified portion of a host fluid. Such a flow configuration is representative of shear instabilities and turbulence in the daytime atmospheric boundary layer and overlying convection-driven part of the troposphere exciting the stably stratified region above the tropopause (Townsend 1965, 1968). It also is representative of equivalent motions in the oceanic mixed layer (Wijesekera & Dillon 1991; Moum *et al.* 1992) exciting the thermocline below it. Although fundamentally different from the emission of IGWs from a turbulent source embedded in a background stratification, where the turbulence follows a well-defined lifecycle (see § 1.2), IGW radiation from a well-mixed region has specific aspects which can provide critical insights into its fully stratified counterpart.

Linden (1975) studied the deepening of a mixing layer created at the top of a stratified water tank by a vertically oscillating grid. Phase-line-tilt angles, defined as the angle between the constant phase lines within a IGW and the vertical direction, of the waves radiated from the base of the mixed layer into the underlying stratification were found to have values of $\theta \approx 35^\circ$.

In a subsequent study, Sutherland & Linden (1998) examined experimentally and numerically the excitation of IGWs by an unstable shear layer within a very weakly stratified layer overlying a stratified bottom layer. The phase-line-tilt angles were found to be in the 45–60° range. The momentum transported by the waves led to deceleration of the mean flow by approximately 7 % of its characteristic flow speed. The accompanying two-dimensional direct numerical simulations (DNS) provided evidence that IGW radiation is indeed correlated with significant changes in the mixed region dynamics. As a result, Sutherland & Linden hypothesized that the dominance of IGW excitation at 45° is the end result of a highly nonlinear feedback between the waves and the turbulence in the mixed region which maximizes the drag on the associated mean flow. After observing turbulence-radiated IGWs prevailingly propagating along a 45° angle in both a shear-free mixed layer (Dohan & Sutherland 2003, 2005) and a turbulent wake of a towed laboratory-scale topography (Aguilar, Sutherland & Muraki 2006; Munroe & Sutherland 2008), Sutherland and coworkers ultimately concluded that the properties of turbulence-generated IGWs are universal; that is, independent of the details of the turbulent source.

Taylor & Sarkar (2007) performed large-eddy simulations (LES) of a turbulent bottom Ekman layer which excited IGW radiation into an overlying stratification. The radiated IGWs had phase-line tilt angles in the 35–60° range. A viscous decay-based model was developed which predicted the rapid decay of high- and low-frequency components of the initial wave spectrum whose content was dictated by the boundary layer turbulence. Far from the turbulent source, the wave spectrum eventually peaked around a dominant frequency set by the requirement of minimal viscous decay along the IGW propagation path. The DNS of Pham, Sarkar & Brucker (2009) of an unstable shear layer provided further support for the above viscous decay model; near the generation site, a relatively broad spectrum of propagation angles was observed, whereas, far from it, they found that the wave propagation angle was concentrated around 45°. Finally, 10 % of the initial shear layer momentum was estimated to be transported away by the radiated IGWs.

1.2. *IGW radiation by localized stratified turbulence: stratified turbulent wakes*

1.2.1. *The non-equilibrium regime in stratified wake evolution*

The stratified turbulent wake of a towed sphere has emerged as the preferred prototype to investigate IGW emission by a localized turbulent region embedded in a background stratification. The fundamental difference between this flow configuration and the well-mixed source set-up considered in the previous section is that the wave-generating turbulence is directly influenced by buoyancy and subject to a distinct lifecycle (Itsweire *et al.* 1993; Spedding 1997). In the parlance of stratified turbulent wakes, IGW radiation is focused in the non-equilibrium (NEQ) regime of wake evolution (Spedding 2002). During this regime, the initially three-dimensional (3D) turbulence is subject to a complex adjustment to buoyancy effects before the flow ultimately transitions into the quasi two-dimensional (Q2D) regime where the vertical velocity field is negligible (Spedding 1997). As conjectured by Spedding (1997), restratification effects are responsible for converting the available potential energy, created by turbulence-induced overturning, into mean kinetic energy, as evidenced by reduced decay rates in the mean velocity defect (Gourlay *et al.* 2001; Dommermuth *et al.* 2002; Brucker & Sarkar 2010; Diamessis, Spedding & Domaradzki 2011).

In parallel, during the NEQ regime, some fraction of the wake's energy is radiated out by IGWs into the ambient fluid. While the mean wake profile continues to spread in the lateral direction with the same growth rate as its unstratified counterpart, the wake height remains locked at the value corresponding to the onset of the NEQ regime. In other words, the wake does not collapse, as proposed by other studies (Gilreath & Brandt 1985; Voisin 1991, 1994). Instead, within the wake, the vertical vorticity is concentrated in slowly evolving quasi-horizontal 'pancake' vortices. The horizontal vorticity is organized in highly diffuse and stable inclined layers (Spedding 1997, 2002; Diamessis *et al.* 2011). The inclination of these layers is a result of straining by the mean velocity field (Spedding 2002). The layering, however, of the horizontal vorticity is strictly an effect of buoyancy, which provides stronger compressive strain in the vertical and biases the flow towards enhanced vertical velocity gradients (Smyth 1999; Diamessis & Nomura 2000). No such vorticity layering is observed in a turbulent flow in a non-stratified fluid (Gourlay *et al.* 2001). Hence, throughout this text, we will refer to the shear associated with these inclined layers as 'buoyancy-driven'.

Both the quasi-horizontal pancake vortices and inclined shear layers are the dominant flow structures upon entry into the Q2D regime. For a given buoyancy frequency, N, this transition occurs at $Nt \approx 50$ according to the lower-Reynolds-number experiments of Spedding (1997). By this point, a balance between the centrifugal force of the pancake eddies and the density and pressure fields is responsible for a nearly undisturbed isopycnal field (Bonnier, Bonneton & Eiff 1998); any remaining IGW radiation has diminished significantly with respect to that which has occurred during the NEQ regime.

More recently, Diamessis *et al.* (2011, referred to herein as DSD) observed a visible prolongation of the NEQ regime with increasing sphere Reynolds number $Re = UD/\nu$, where U and D are the sphere tow speed and diameter and ν is the kinematic viscosity. This prolongation is intimately linked to the destabilization of the above inclined shear layers, whose thickness was found to decrease with Re whereas their magnitude increased. To this effect, secondary Kelvin–Helmholtz (K–H) instabilities and turbulence were observed up to $Nt \approx 100$ for $Re = 10^5$. The persistent strong displacement of isopycnal surfaces induced by these secondary turbulent events is very likely to drive IGW radiation over much longer intervals than those corresponding to

laboratory experiments, which are conducted at Re typically an order of magnitude lower. A number of theoretical, laboratory and numerical studies, reviewed below, have examined the IGW emission by a stratified turbulent wake, although none has specifically examined the effect of Re on this phenomenon.

In the remainder of this manuscript, we differentiate between 'low' and 'high' Re stratified turbulent wakes. High-Re stratified wakes are those which have an Re that is sufficiently high, such as the value considered by DSD or even higher. Above this limit Re, the above secondary K–H instabilities and turbulence occur within the wake core. This set of distinct physical processes operating inside the wake core, linked to the secondary phenomena, is absent in a low-Re stratified wake where any turbulence inside the wake core is rapidly suppressed early into the NEQ regime. DSD showed that the magnitude of the above buoyancy-driven shear layers scales as Re/Fr^2, where $Fr = 2U/(ND)$ is an internal Froude number. Therefore, at even higher Re, buoyancy-driven shear intensifies even further leading to even stronger secondary events and a longer NEQ regime.

1.2.2. *Laboratory experiments*

The early shadowgraph-image-based experiments of Gilreath & Brandt (1985) of a self-propelled body inside a stably stratified fluid distinguished two types of IGW observed in the wake of the body: (*a*) deterministic, repeatable in apparently identical realizations of the experiment, body-generated/lee waves and short-lived transient waves generated by the swirling motion of the propeller; and (*b*) non-deterministic IGWs, characterized as random by the authors, that are emitted by the turbulent wake emerging during what is regarded as a wake collapse. This collapse was proposed to occur once the large-scale turbulent bursts/puffs on the wake boundary cease to grow on account of the continuously increasing influence of buoyancy forces in the downstream direction.

The turbulent kinetic energy of the wake was hypothesized to be transferred into available potential energy and hence to random IGWs when a local turbulent Froude number, based on the r.m.s. turbulent velocity and the turbulent integral scale, approaches unity. Linear theory was found to successfully predict the amplitude of the deterministic component of the IGW field but not that of the random component on account of its highly complex turbulent wake source (see § 1.2.1).

Bonneton, Chomaz & Hopfinger (1993, referred to herein as BCH) used a custom-designed laser-induced fluorescence technique (Hopfinger *et al.* 1991) to measure the IGW-driven isopycnal displacement on a horizontal plane beneath the turbulent wake core. Over the range of sphere-based Reynolds numbers, $Re \in [380, 3 \times 10^4]$, considered, the observed IGW field transitioned from a lee-wave-dominated to a random-wave-dominated field at $Fr \approx 4.5$, independent of Re. At the same Fr, IGW emission persisted for a much longer time when Re was increased by a factor of ten.

BCH also suggested that the random IGW wavelength decreases roughly as $1/Nt$, in agreement with impulsive source theory (Lighthill 1978; Zavol'Skii & Zaitsev 1984; Voisin 1991, 1994). Nonetheless, their results are subject to large scatter and visual inspection of their cloud of data points suggests an actual decrease at a rate quite slower than $1/Nt$. Moreover, when one graphically computes the slope of the line tangent to the top and bottom edge of the cloud of data points in figure 8 of BCH, a power law of Nt^{α} with $\alpha \in [-0.4\ -0.7]$ is inferred.

The waves arriving first at the measurement plane of BCH had a horizontal wavelength of $\lambda_H \in [1.5D, 2D]$ with a phase-line tilt angle of $\theta = 55^{\circ}$. Such a value of θ maximizes the wave-induced isopycnal displacement amplitude according to

Lighthill's theory for IGWs generated by a point disturbance. In this regard, when a model of a mixed region collapsing in a uniformly stratified fluid is considered as wave source, the solution of the linearized IGW equations shows that the isopycnal displacement amplitude of the radiated IGWs is maximized along $\theta = 38^\circ$ (Meng & Rottman 1988). However, this model is rather unlikely to be applicable to the wake of a towed sphere because of the relatively weak mixing observed inside the wake (cf. Brucker & Sarkar 2010).

Robey (1997) towed a sphere along the base of the thermocline of a two-layer fluid. Results from a numerical model, based on the linearized equations of motion, where sphere and wake motion were represented by a distribution of sources and sinks, were also examined. For the wake-generated random waves, the source was assumed to be a large-scale turbulent eddy with characteristic scales (velocity, length and diameter) that were estimated on the basis of resonance between the eddies and the stratification. The model produced reasonable agreement with the experimentally determined wave displacement amplitude.

Spedding *et al.* (2000) examined the structure and properties of the IGW field radiated by a towed sphere in a linearly stratified fluid. Two-dimensional wavelet transforms were used to analyse particle image velocimetry (PIV) data sampled on a horizontal plane above the wake centreline. An $Fr^{1/3}$ scaling, derived from the evolution of the average horizontal eddy dimensions (Spedding, Browand & Fincham 1996), was found to partially collapse the time series of horizontal wavelengths.

1.2.3. *Theoretical models*

Beyond the theories that successfully predict the geometry of body-generated deterministic waves and the waves generated by a moving point source (Miles 1971; Peat & Stevenson 1975; Lighthill 1978; Chashechkin 1989) in a stratified fluid, two sets of theoretical studies provide a preliminary explanation of the origin of the random component of the IGW field from within the turbulence along with a prediction of some its spectral characteristics. Relying on a spectrally based theory for the lifecycle of a stratified turbulent patch, Gibson (1980) suggested that large-scale turbulent eddies transfer their kinetic energy to IGWs when the largest isopycnal overturning scale inside the patch is equal to the Ozmidov scale,

$$L_O \equiv (\epsilon/N^3)^{1/2}, \tag{1.1}$$

where ϵ is the turbulent kinetic dissipation rate (Dougherty 1961; Ozmidov 1965). This transition point in the evolution of a stratified turbulent patch is regarded as the 'beginning of fossilization' by Gibson or 'onset of buoyancy control' by others (Itsweire *et al.* 1993). It effectively corresponds to the beginning of the NEQ regime in the evolution of a stratified turbulent wake (Spedding 1997). According to Gibson, the patch-radiated waves have a wavelength equal to the value of L_O at this time and a frequency close to N.

The experimental studies of Wu (1969) and Gilreath & Brandt (1985), and their claim that the collapse of individual density/velocity disturbances in a stratified fluid may serve as impulsive sources of IGWs, served as the springboard for the theoretical work by Voisin (1991, 1994). Voisin thus modelled IGW radiation from a turbulent wake as a process driven by a discrete distribution of impulsive sources and sinks which are periodically spaced in both space and time and represent a collection of turbulent puffs resulting from the collapse of connected vortex loops within the wake. The theory predicted that the wavelength of an IGW decreases as $1/Nt$ and that the phase-line-tilt angle $\theta = 55^\circ$ maximizes wave displacement amplitude that itself

increases according to $\sqrt{Nt}$. However, the theory did not predict the value of the wavelength itself or its possible Re and Fr scaling.

Finally, a relevant study is that by Plougonven & Zeitlin (2002) on IGW emission from an idealized inviscid pancake vortex model which exploits similarities with sound wave emission by unsteady vortex motion in a compressible fluid (Lighthill 1952). In this model, wave emission was found to have a significant impact on the source vortex, eventually leading to its destabilization.

1.2.4. *Numerical simulations*

Only a limited number of computational studies have considered the IGW field radiated by localized turbulence in a stratified fluid. Druzhinin (2009) performed numerical simulations of a stratified jet. Two values of Reynolds number, based on the jet diameter and centreline velocity, of 400 and 700 were considered at very low $Fr \in [0.3, 2.5]$. Graphical estimates from two-dimensional transects yielded a phase-line tilt angle of 53° to the vertical.

Finally and more recently, de Statler, Sarkar & Brucker (2010) performed DNS of a stratified turbulent wake at $Re = 10^4$, where three values of Prandtl number, $Pr = \nu/\kappa = 0.2, 1$ and 7 were examined (where κ is the mass diffusivity). At the lowest value of Pr, the enhanced diffusion within the density field caused a significant reduction in IGW energy flux into the ambient. In contrast, only subtle variation was observed in the IGW energy flux for the more geophysically relevant values of $Pr = 1$ and 7.

1.3. *Outstanding issues*

Despite the valuable insights provided by previous studies on the wake-radiated IGW field, a number of critical aspects of this phenomenon have not yet been addressed. The localization of the wake in the transverse direction manifests itself in an equivalent localization of the wake-radiated IGW field on any observation plane vertically offset sufficiently far from the wake centreline. Estimation of the spectral properties of the IGWs is realizable a lot more efficiently by using the wavelet transforms and their localized basis functions, which provide output in both physical and spectral space (Dallard & Spedding 1993).

The pioneering experimental studies of Gilreath & Brandt (1985) and BCH reported quantitative IGW data at only a few isolated locations in their experimental facilities. The variation in properties of the IGW field in the transverse and vertical direction, resulting from its corresponding inhomogeneity, needs to be explored while exploiting the associated streamwise homogeneity to extract reliable statistical descriptions of the quantities of interest.

Additionally, a broader range of Re and Fr values over which random waves dominate the radiated IGW field needs to be examined. On one hand, on account of restrictions of the associated experimental facilities, BCH and Robey (1997) limited their Fr to the intervals $[4.5, 12.7]$ and $[4, 22]$, respectively. On the other hand, Gilreath & Brandt (1985) considered only one Fr value. Spedding *et al.* (2000) examined a broader range of Fr but provided only a preliminary analysis of the radiated IGW field. In a similar vein, presumably constrained by limitations in the experimental facility (BCH; Spedding 1997), the above laboratory studies were not able to significantly vary Re. The numerical studies of Druzhinin (2009) and de Statler *et al.* (2010) were also restricted to a relatively low Re value. As indicated in § 1.2.1, the prolongation of the NEQ regime at higher Re has implications for various aspects of wake structure and dynamics.

1.4. *Objectives and basic questions*

Motivated by the above discussion, the primary objective of this study is to characterize the IGW field over a range of Re and Fr that is considerably broader than that considered in previous studies. To this end, it is of primary interest to determine whether the extended duration of the NEQ regime at high Re results in a prolongation of IGW radiation, through the persistent excitation of the isopycnals by secondary turbulence. Note that hereafter any reference to persistent excitation of isopycnals or persistent IGW radiation indicates that these phenomena last much longer than they do in low-Re wakes.

In addition, on account of the dynamically evolving turbulent wake structure during the NEQ regime, this work aims to assess the potential impact of increased Re, and the increasingly inviscid dynamics inside the wake, on the spatial structure, wavelengths, frequencies and amplitudes of IGWs in the near field. Although the spectral properties of the radiated waves far from their source are critically important, simulations which can accurately resolve both the wake turbulence and the far field of radiated IGWs are prohibitively costly and deferred to future studies.

Some specific questions include: Is IGW radiation a transient phenomenon, in the form of short-lived impulsive bursts, or does it occur in a more continuous/quasi-steady manner? If the latter is true, is it dependent on the duration of the NEQ regime (or Re for that matter)? What is the dependence of IGW wavelength magnitude and its rate of decrease on Re and Fr? Is there any plausible Re and Fr scaling for these wavelengths that is traceable to a corresponding scaling for the turbulent source characteristics? Do the IGW wavelengths decrease in agreement with the impulsive source theory? Does the preferred IGW phase-line tilt angle change with increasing Re and, if yes, does such a change denote a transition from a wave radiation process that is viscously controlled to a more inviscid one that maximizes momentum extraction from the wake?

2. Model formulation

The base flow considered in this study is identical to that considered in DSD. This section discusses the most important features of base flow geometry. The reader interested in more detail, especially in the context of design and implementation of initial conditions, is referred to DSD. The few subtle differences in simulation set-up between this work and DSD are discussed at the end of § 4.

Specifically, we examine a stratified turbulent wake with non-zero net momentum. Such a flow corresponds to the wake of a sphere of diameter D towed with a velocity U in a uniformly stratified fluid with buoyancy frequency N; see figure 1. As implemented by Orszag & Pao (1975) and in more recent studies of stratified turbulent wakes (Gourlay *et al.* 2001; Dommermuth *et al.* 2002; Diamessis, Domaradzki & Hesthaven 2005; Brucker & Sarkar 2010, DSD), on account of challenges of computational complexity, the computational domain and spatial discretization do not account for the sphere and focus only on the flow generated in its wake. Specifically, the computational domain is a fixed three-dimensional volume, of dimensions $L_x \times L_y \times L_z$, inside the wake region centred on the wake centreline. The sphere is considered to have already travelled through the computational domain, moving in the rightward direction. The wake centreline corresponds to $(y/D, z/D) = (0, 0)$. Within the computational domain, the three-dimensional and time-dependent wake flow field is computed by solving the incompressible Navier–Stokes equations under the

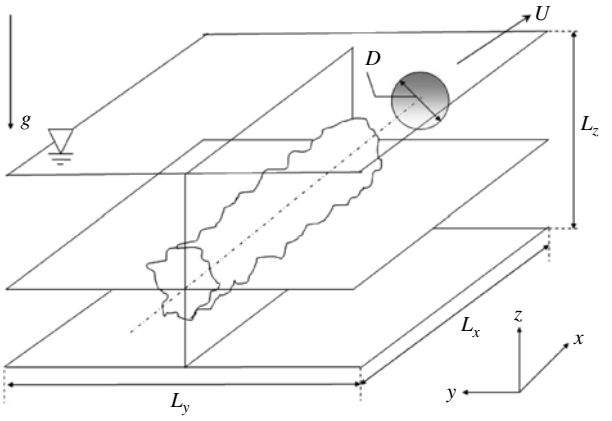

FIGURE 1. Computational domain for the simulation of a stratified turbulent wake with non-zero net momentum. The wake centreline is located at $(y/D, z/D) = (0, 0)$.

Boussinesq approximation:

$$\frac{\partial \boldsymbol{u}}{\partial t} = -\frac{1}{2}[\boldsymbol{u}\cdot\nabla\boldsymbol{u} + \nabla(\boldsymbol{u}\cdot\boldsymbol{u})] - \frac{1}{\rho_0}\nabla p' + \nu\nabla^2\boldsymbol{u} + \boldsymbol{F}_g, \tag{2.1}$$

$$\frac{\partial \rho'}{\partial t} = -\nabla\cdot(\boldsymbol{u}(\rho' + \overline{\rho}(z))) + \kappa\nabla^2\rho', \tag{2.2}$$

$$\nabla\cdot\boldsymbol{u} = 0. \tag{2.3}$$

where

$$\boldsymbol{F}_g = -g\frac{\rho'}{\rho_0}\hat{\boldsymbol{k}}. \tag{2.4}$$

Note that $\boldsymbol{u}$ is the three-dimensional instantaneous velocity vector, $\overline{\rho}$ is a mean density $\overline{\rho}$, and ρ_0 is a reference density. The quantities p' and ρ' are the perturbations of the pressure and the density from the corresponding sum of mean and reference values, which are in hydrostatic balance (Diamessis *et al.* 2005).

The boundary conditions used in the numerical model are periodic in the horizontal direction. In the vertical direction, free-slip and zero-flux for the velocity and density, respectively, are used. The computational model thus represents a flow domain sufficiently removed from the free surface and bottom boundary of the water column. This representation no longer holds when wake-radiated internal waves spuriously re-enter from the periodic spanwise boundaries or reflect from the impermeable vertical boundaries. To prevent such spurious effects, artificial wave-absorbing layers (Klemp & Lilly 1978; Israeli & Orszag 1981; Durran 1999) that wrap around the vertical and spanwise boundaries and extend along the full length of the domain are used. Numerically, this is accomplished by adding negative forcing terms to the right-hand side of (2.1) and (2.2) that act to rapidly damp out wave motion within a relatively short distance inside such layers. Details on sponge layer formulation and implementation may be found in Abdilghanie (2010). A sponge layer thickness of $2D$ for $Fr = 4$ and 16, at both values of Re considered, and a thickness of $4D$ for $Fr = 64$ are found to be adequate to minimize spurious reflections from the sponge layers.

The numerical method used to generate the stratified wake results analysed in this paper is an MPI-parallelized spectral multidomain penalty-method model developed

to simulate incompressible high Reynolds-number localized stratified turbulence in horizontally periodic and vertically finite domains. Details on the numerical model may be found in Diamessis *et al.* (2005) and DSD. Through the multidomain scheme, resolution is concentrated on the wake core and the larger-scale turbulent motions within it, which include the secondary K–H instabilities and turbulence at high Re that sustain persistent IGW radiation. Away from the wake core, the subdomain thickness becomes larger, though adequate to resolve the relevant length scale of interest, the vertical wavelength of the IGW field which is $O(D)$.

3. Continuous wavelet transform (CWT)

The Fourier transform, on account of its globally defined periodic basis functions, is best suited for (nearly) monochromatic signals where the spectral content of the signal does not change over space or time. It has proven useful in previous analyses of IGW fields emitted from forced turbulent sources (Sutherland, Flynn & Dohan 2004; Aguilar & Sutherland 2006; Taylor & Sarkar 2007; Munroe & Sutherland 2008). However, it is of limited use for wave fields whose frequency (wavenumber) content changes over time (space). The localized nature of the wake-generated IGW field is due to the spatial localization of the wake core itself in the vertical and transverse directions and the finite duration of any vertical turbulent motions within the wake due to buoyancy-driven decay (Diamessis, Gurka & Liberzon 2010). The temporal localization is mainly evident in low-Re wakes.

In one dimension, the CWT of a continuous temporal signal $x(t)$ with respect to a wavelet basis function (or mother wavelet) $\psi(t)$ is defined as

$$T(a,b) = \frac{1}{\sqrt{a}} \int_{-\infty}^{\infty} x(t)\psi^* \left(\frac{t-b}{a} \right) \mathrm{d}t, \tag{3.1}$$

where the asterisk denotes the complex conjugate of an analysing wavelet that is obtained from a mother wavelet $\psi(t)$ through translation to a location b and stretching by a factor a. By virtue of its localized basis functions, the CWT retains information in both physical and spectral domain at optimal resolution (Dallard & Spedding 1993). Large values of the CWT modulus $T(a,b)$ signify resonance between signal and the analysing wavelet at the corresponding scale.

The wavelength of the IGWs is extracted using either of two complex two-dimensional wavelet basis functions as defined by Dallard & Spedding (1993). The first mother wavelet, Morlet2D, is direction-specific. It selects localized wavenumber vectors with a preferred magnitude and orientation. The second wavelet basis function, Arc, is regarded as cylindrical; it has no directional selectivity and hence resonates with wavenumber vectors of a particular magnitude regardless of orientation. Finally, the one-dimensional CWT based on the complex Morlet wavelet (Addison 2002) is used to extract the frequency content of time series obtained at multiple spatial locations.

4. Summary of numerical simulations

This study considers results from five different numerical simulations: at Reynolds number $Re = 5 \times 10^3$ for Froude number $Fr = 4, 16$ and 64, and at $Re = 10^5$ for $Fr = 4$ and 16. DSD examined the same parameter values, augmented by one more simulation at $Re = 10^5$ and $Fr = 64$. Hereafter, each run is labelled as RxFy, where $x = Re/10^3$ and $y = Fr$. As in DSD, for all simulations, the values of U and D are the

same. The Reynolds number and Froude number are varied by changing the values of ν and N, respectively.

All simulations are run up to $Nt = 100$, by which time, at low Re, the wake core is well within the Q2D regime (Spedding 1997, DSD;). At high Re, very few secondary K–H instabilities survive beyond $Nt = 100$ (DSD), at which point IGW radiation begins to significantly diminish.

To unambiguously determine the IGW-field spectral characteristics, the computational domain dimensions should be large enough to allow adequate distance for the IGWs to freely propagate away from the wake core, thereby preventing any contamination of the wave field analysis by the wake turbulence. At $Fr = 4$ and 16, for both Re, the domain in this study has dimensions $L_x \times L_y \times L_z = 26(2/3)D \times 26(2/3)D \times 12D$. The $Fr = 64$ case uses domain dimensions of $26(2/3)D \times 40D \times 20D$ to account for a broader and taller wake during the time intervals of interest.

The choice of the dimensions of the domain in this study is sufficient to enable reliable estimation of the near-field properties of the radiated IGW field and direct comparison of our results to the experiments of BCH. 'Near field' here denotes that the IGW field is sampled at locations which range between one to two sphere diameters away from the vertical location of the edge of the turbulent wake, estimated based on the wake half-height values provided by DSD. Investigating the far-field properties of the IGWs requires much deeper domains giving rise to a significant and prohibitive increase in computational cost.

Across all runs, the computational grids are nearly identical with those used by DSD for the equivalent parameter values (see their figure 3 for an example). For both $Fr = 4$ and 16, the resolutions at $Re = 5 \times 10^3$ and 10^5 are $256 \times 256 \times 175$ and $512 \times 512 \times 531$ mesh points, respectively. In this regard, the only difference with DSD is the use of double the number of mesh points, though equal resolution per unit length, in the spanwise direction with respect to DSD. The $Re = 5 \times 10^3$ and $Fr = 64$ case uses a resolution of $256 \times 384 \times 225$ to accommodate a taller and deeper domain. An equivalent increase in resolution at $Re = 10^5$ for $Fr = 64$ requires an increase in resolution that exceeds the memory capacity per processor of the Arctic Region Supercomputing Center's Midnight cluster used to perform the simulations considered here. We have thus deferred such a simulation to future, longer-term, efforts. Finally, the spectral filters used for each value of Re and Fr are the same as those employed by DSD (see their figure 4).

Adequate resolution of the turbulent wake core for all the simulations considered here has already been demonstrated in DSD, both in terms of the scale of the inclined shear layers and the resulting primary two-dimensional stage of the Kelvin–Helmholtz instabilities and subsequent billow pairing. For details, see the relevant discussion on pp. 68 and 78–79 of that paper. Therefore, any IGW-generating motions inside the wake core are well-resolved. Moreover, the IGW wavelengths, as computed in § 5.2 below and inferred from the visualizations of figures 3–6, are also well-resolved.

Finally, we emphasize that subtle differences exist between the simulations reported here and those reported in DSD. The simulations considered in this paper use wider and, for $Fr = 64$, deeper domains than DSD. In addition, sponge layers wrap around the lateral and top/bottom boundaries of the domain. The simulations are run only up to $Nt = 100$, times where IGW radiation is significant for the higher Re considered. The regridding used by DSD is not employed here. Whereas the regridding strategy used by DSD enabled them to run as far as $Nt \approx 2000$, the lack of sponge layers in their simulations and the application of the first regridding at times where the radiated

IGWs had already re-entered from the periodic boundaries do not allow a reliable examination of the IGW field in the DSD dataset.

5. Results

5.1. *Visualization of the wave field structure*

Following the preliminary study of Spedding *et al.* (2000), the fundamental quantity in the visualization and analysis of the wake-radiated IGW field performed here is the horizontal divergence of the velocity field

$$\Delta_z \equiv \nabla \cdot \boldsymbol{u}_H, \tag{5.1}$$

where $\boldsymbol{u}_H \equiv (u, v)$ is the horizontal velocity vector. If Fr_l represents a local Froude number, based on the local integral scale of the turbulence and the r.m.s. of the velocity fluctuations, then in the very low-Fr_l limit, as indicated by Spedding *et al.* (1996) and according to the decomposition of Riley, Metcalf & Weissman (1981) and Lilly (1983), Δ_z enables an exact separation of internal wave motions with time scales of $O(N^{-1})$ and amplitudes in z of $O(1)$ from turbulent motions, namely vortical modes, with time scales $O(N^{-1}/Fr_l)$ and vertical motion of amplitude $O(Fr_l^2)$ in z. In the flows considered here, even if Fr_l may be relatively large at early times, indicating a weak influence of buoyancy, it eventually attains a small value signifying full buoyancy control over the turbulent motion inside the wake. Thus, Δ_z is an approximate, though highly convenient, descriptor of the IGW field.

Δ_z may be related to the IGW-driven vertical isopycnal displacement amplitude field in a straightforward way. For small-amplitude IGW field with horizontal and vertical wavenumbers, κ_H and m, and frequency ω in a uniformly stratified fluid (Sutherland 2010),

$$|A_\zeta| = \frac{|A_{\Delta_z}|}{m\omega}, \tag{5.2}$$

where A_{Δ_z} is the amplitude of the horizontal divergence field and A_ζ is the isopycnal displacement amplitude. Since the vertical wavenumber is related to the horizontal one by $m = \kappa_H \tan(\theta)$ and by virtue of the linear internal wave dispersion relation, $\omega = N\cos(\theta)$, the isopycnal displacement amplitude is therefore proportional to A_{Δ_z}/N. Moreover, for IGWs subject to a relatively narrow range of propagation angles, the factor $\kappa_H \tan(\theta)\cos(\theta)$ may be treated as constant. Therefore, normalizing the horizontal divergence field by the buoyancy frequency then provides an approximate measure for the isopycnal displacement of the wave field.

In the remainder of this paper, any discussion of IGW-induced isopycnal displacement will be limited to qualitative assessment of the visualizations pertinent to this section. The wave steepness, a measure of wave nonlinearity (Sutherland 2010), may be readily obtained by normalizing the maximum isopycnal displacement by the horizontal wavelength of the IGW. More quantitative analysis of the steepness of the IGW field examined here is the subject of ongoing research. For preliminary results on the evolution of wave steepness in the simulations considered here and the implications of these results for the potential for destabilization of the radiated IGWs (Sutherland 2001), the interested reader is referred to Abdilghanie (2010).

Figure 2 shows the evolution in time (in buoyancy units) of the complex three-dimensional structure of the normalized horizontal divergence field at $Fr = 4$ and 16 at $Re = 5 \times 10^3$, and $Fr = 4$ at $Re = 10^5$. These snapshots and full animations (not shown here) confirm that coherent IGW packets with a fairly well-defined spatial

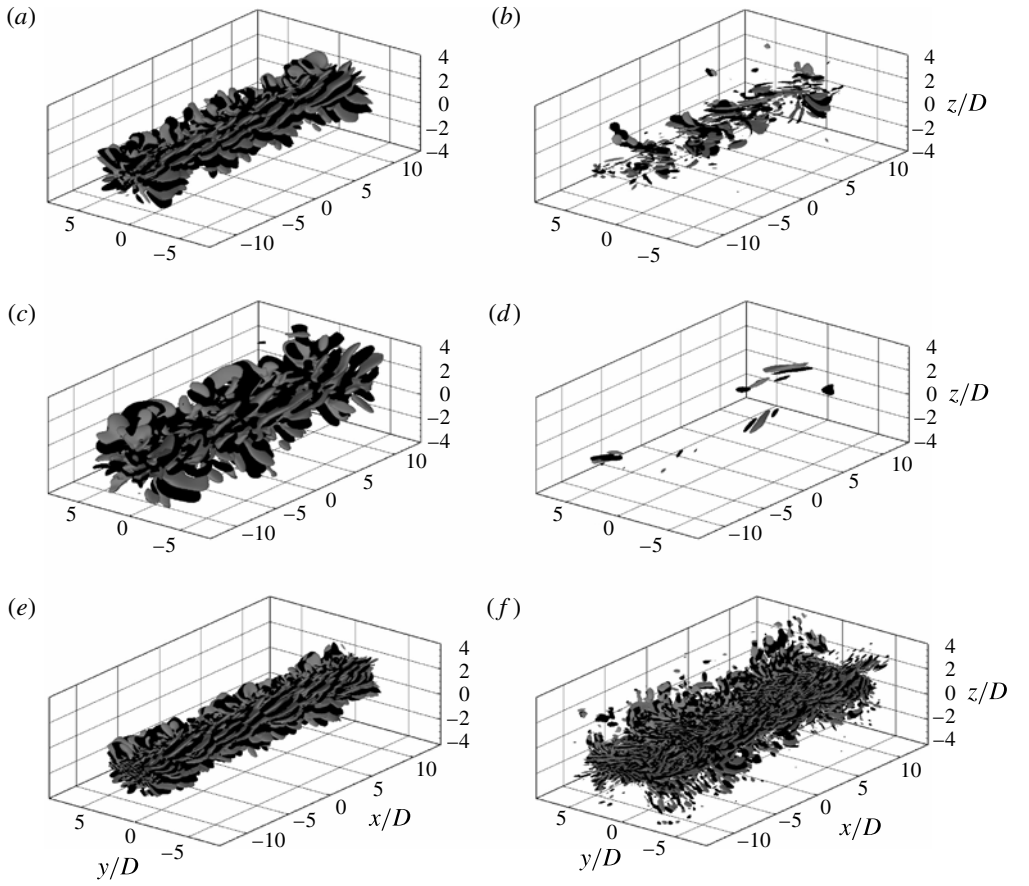

FIGURE 2. Three-dimensional isosurface plot of Δ_z/N at $Nt = 20$ (*a*,*c*,*e*) and $Nt = 50$ (*b*,*d*,*f*) for (*a*,*b*) R5F4, (*c*,*d*) R5F16, (*e*,*f*) R100F4. The sphere travels from left to right. Isosurface values of Δ_z/N are sampled at (*a*,*b*) ± 0.025, (*c*,*d*) ± 0.04, and (*e*,*f*) ± 0.05.

orientation are continuously radiated by the turbulent wake throughout the NEQ and early Q2D regimes, suggesting that the source of the waves has a more persistent nature, as opposed to the impulsive radiation model proposed by BCH and Voisin (1991, 1994). Furthermore, the appearance of wavepackets at random locations at different times suggests that, if an approximate impulsive source model for the wave generation process is to be constructed, it will have to incorporate many such sources with possibly random separations in space and time.

At low Re, as Fr is increased, an increase in the horizontal wavelength, λ_H, of the waves is discernible. In contrast, the spatial density of the IGW field is reduced as is also the persistence in its emission. The reduced duration in buoyancy units of IGW radiation with increasing Fr may be attributed to the turbulent wake core having evolved a longer downstream distance (in x/D units) and, thus, having undergone greater viscous decay, at these low Re (Spedding 1997, DSD). Note that by $Nt = 50$, the time of transition from NEQ to Q2D regimes at lower Re values typical of the laboratory (Spedding 1997, DSD), a few weak and disperse IGW packets survive at $Fr = 4$, whereas at the two higher $Fr = 16$, and 64 (not shown), no IGWs of

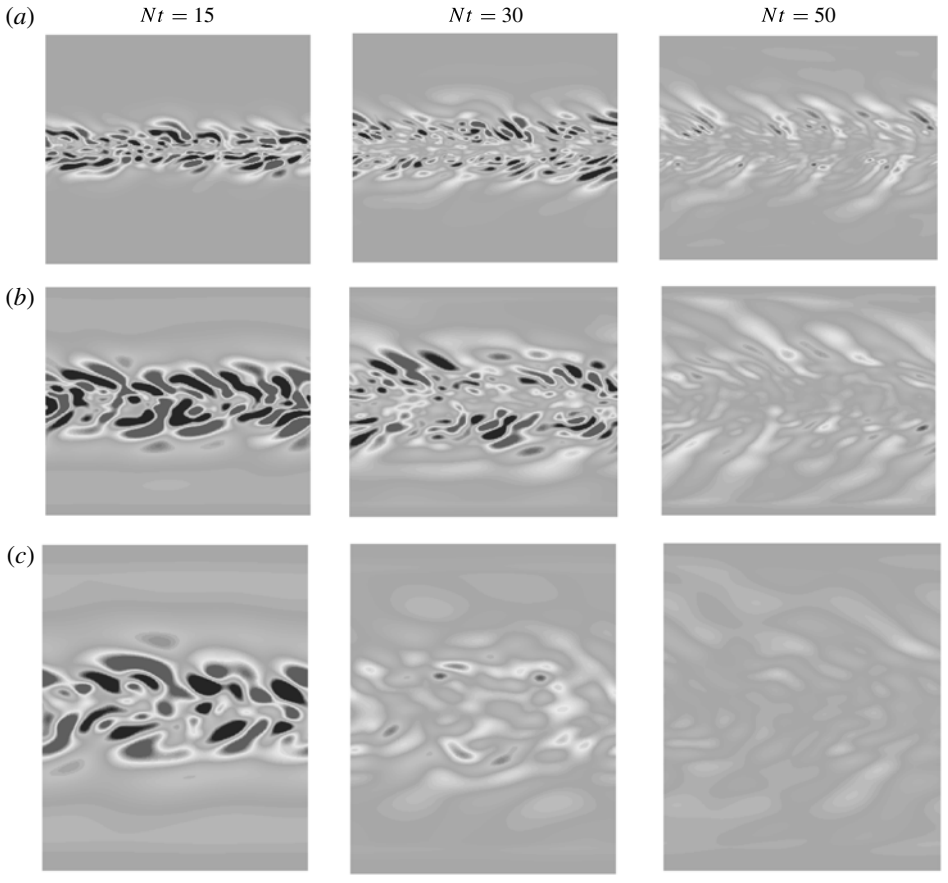

FIGURE 3. Two-dimensional contour plot of Δ_z/N at different times on horizontal xy-planes at $z/D = 1.5, 2.3, 3.4$ for respectively (a) R5F4, (b) R5F16, (c) R5F64. The minimum/maximum ranges for the colourbars of Δ_z/N are (a) [−0.025, 0.025], (b) [−0.04, 0.04] and (c) [−0.05, 0.05]. The dimensions of the visualization window are equal to the full horizontal dimensions of the computational domain for the particular Fr.

any meaningful amplitude are observed. Beyond this point, any IGWs radiated by the wake core may be attributed to the slow oscillations of the pancake vortices prevalent in the Q2D regime (Plougonven & Zeitlin 2002; Spedding 2002) and not any residual/adjusting turbulence characteristic of the NEQ regime.

As Re is increased, persistent IGW radiation is still observed up to $Nt = 80$ and the spatial density of the IGW field increases relative to the lower-Re cases. As time advances, IGW wavelengths decrease and the radiated wave field appears to have a less organized spatial structure. These observations confirm that the prolongation of the NEQ regime observed by DSD is accompanied by a persistence of IGW emission most likely driven by secondary K–H instabilities and the resulting turbulence. As proposed by Spedding (2002), the slow oscillations of the quasi-horizontal pancake vortices, which begin to emerge later in the NEQ regime, may also be a contributing factor, though not the primary one.

Greater detail into the structure of the wake-radiated IGW field can be obtained by considering two-dimensional transects. In terms of both visualization and IGW-field

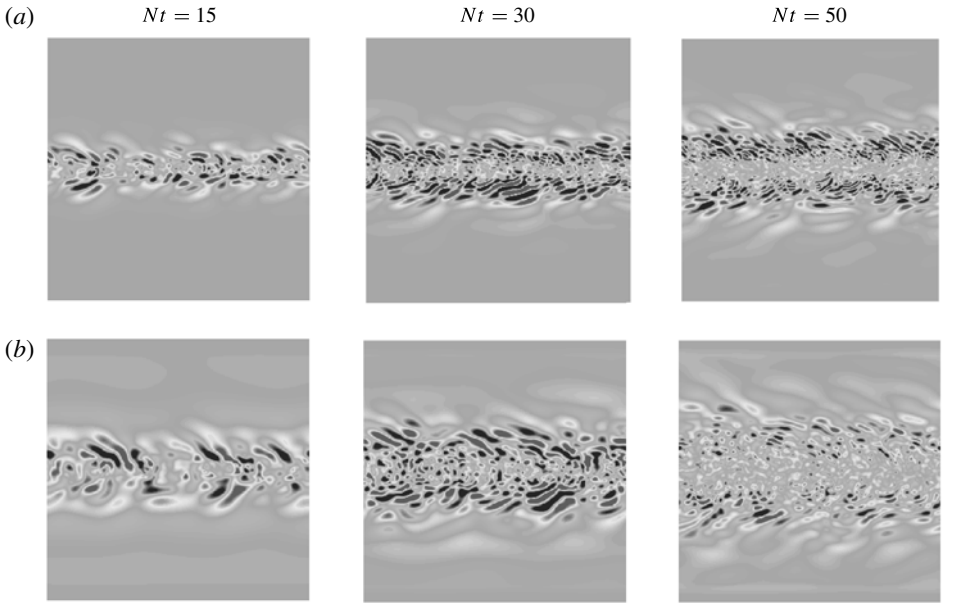

FIGURE 4. Two-dimensional contour plot of Δ_z/N at different times in the range $15 < Nt < 50$ on horizontal xy-planes at $z/D = 1.5, 2.3$, for respectively (a) R100F4, (b) R100F16. The minimum/maximum ranges for the colourbars of Δ_z/N are (a) $[-0.05, 0.05]$, (b) $[-0.075, 0.075]$. For each Fr, the size of the visualization window is the same as in the corresponding $Re = 5 \times 10^3$ contour plots in figure 3.

analysis, we focus on xy-planes vertically offset from the wake centreplane (figures 3–5). These planes are free of motions from the turbulent wake core, are optimal for two-dimensional wavelet analysis (see §§ 3 and 5.2) and enable a straightforward comparison with the experimental results of BCH and Spedding *et al.* (2000). Here, unlike figure 2, we show visualizations from all Re and Fr examined to enable a full comparison of the radiated IGW-field geometry across all values of the governing parameters considered.

According to figure 3, the amplitude of the normalized horizontal divergence field increases with Fr. This increase of amplitude with reduced stratification strength indicates, by virtue of (5.2), that the isopycnal displacement amplitude may also increase. For the same Fr, by contrasting figures 3–5, one also observes a significant increase in the amplitude of the normalized horizontal divergence field with increasing Re.

The evolution and structure of the wave field in figure 3, for $Re = 5 \times 10^3$, is very similar to that observed by Spedding *et al.* (2000) for their $Fr \geqslant 4$ cases where the random wake-generated component dominates the wave field. Consistently with figure 2, at low Re, IGW radiation is a short-lived process; wave emission begins early in the NEQ regime and continues until the flow transitions into the Q2D regime, the approximate transition point identified by DSD. In contrast, at high Re (figures 4 and 5), the emission of energetic IGW packets persists as late as $Nt \approx 90$ and $Nt \approx 70$ for runs R100F4 and R100F16, respectively. For the $Fr = 4$ runs, a corresponding sequence of snapshots at $z/D = 3$ (not shown here) reveals no wave activity up

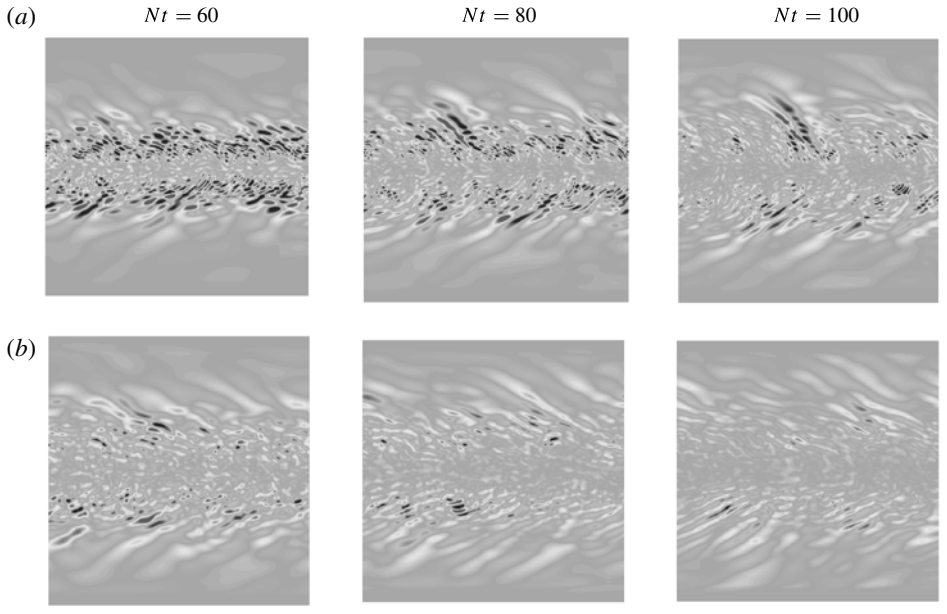

FIGURE 5. Two-dimensional contour plot of Δ_z/N at different times in the range $60 < Nt < 100$ on horizontal xy-planes at $z/D = 1.5, 2.3$, for respectively (a) R100F4, (b) R100F16. The minimum/maximum ranges for the colourbars of Δ_z/N are (a) $[-0.05, 0.05]$, (b) $[-0.075, 0.075]$. The size of the visualization window is the same as in figure 4.

to $Nt \approx 15$ and the arrival of qualitatively similar wake-radiated IGW packets by $Nt \approx 30$ and onward.

The emitted wave field consists of localized wavepackets with clearly defined primary horizontal wavelength, λ_H, and a lateral envelope thickness typically containing one to two such wavelengths. This envelope thickness is reduced as Fr increases, an indication of increased localization of the wavepackets. The trend of λ_H increasing with Fr and decreasing over time, already observed in the three-dimensional visualizations of figure 2, is even more clear in these two-dimensional transects. Moreover, the observed wave packets are increasingly less coherent as time advances, especially at high Re.

The horizontal divergence field on an xz plane, offset in the transverse direction by a distance equal to the vertical offset of the previously examined xy plane, is shown in figure 6. We only show the low-Fr simulations at $Nt = 30$, as the two corresponding snapshots are sufficient for demonstrating any structural features of interest. The orientation of the phase lines is similar to that in the shadowgraph images obtained by BCH (see their figure 10). The wavepackets extend forward in the direction of notional sphere motion (from left to right). Note that the field of view of the PIV images of Spedding (2002) was too confined within the wake core to reveal any orientational preference.

The same forward orientation is observed for IGWs generated by flow over corrugated or isolated topography (Nappo 2002; Aguilar *et al.* 2006) and or IGWs generated by turbulent boundary layers into the free stream (Taylor & Sarkar 2007; Gayen, Taylor & Sarkar 2010). For these types of flow, and the wake as well, the isophase lines are inclined towards the direction of the source velocity relative to the

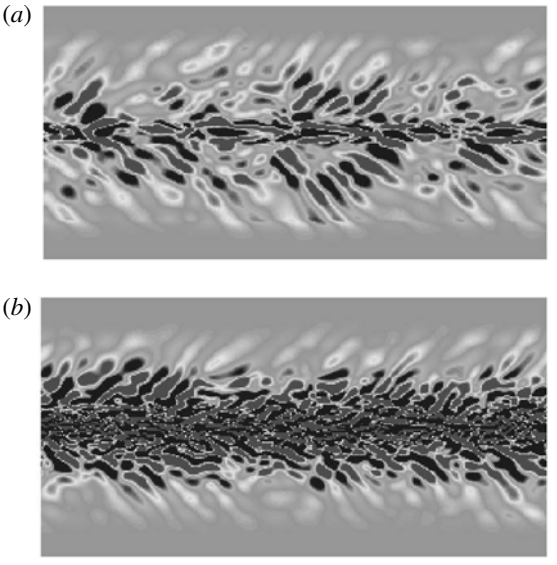

FIGURE 6. Two-dimensional contour plot of Δ_z/N at $Nt = 30$ on the vertical xz-plane at $y/D = 1.5$ for (*a*) R5F4, (*b*) R100F4. The minimum/maximum ranges for the colourbars of Δ_z/N are (*a*) $[-0.025, 0.025]$, (*b*) $[-0.05, 0.05]$. The visualization window has dimensions $26\,2/3D \times 12D$ and is centred around $z/D = 0$.

free-stream velocity. In the case of the wake, given the absence of any currents in the ambient fluid, this direction is that of the mean wake velocity profile, a direct result of the unidirectional forcing by the towed sphere. In other words, the advection of the wake-generating structures by the mean wake profile is the only way by which fore–aft symmetry is broken in this problem (Geoffrey Spedding, personal communication).

Finally, for both simulations at $Fr = 4$, the continued lateral expansion of the wake core is responsible for the emergence in the field of view of figure 6 of either nearly horizontal features, presumably linked to inclined horizontal vorticity layers (DSD), (low *Re*) or small-scale turbulence (high *Re*).

5.2. *Spectral characteristics of the IGW field*

The basis of our analysis of the IGW-field spectral characteristics is the application of two-dimensional wavelet transforms on the horizontal divergence field sampled on xy planes vertically offset above the wake centreline. In each simulation, these analysis planes are those examined in the visualizations of figures 3–5. At a given time, a single two-dimensional xy transect is found to provide sufficient information on the spanwise variability of the wake-radiated IGW field. Details on the computation of the horizontal wavelength via two-dimensional wavelets from the xy transects are provided in appendix A.

5.2.1. *Horizontal wavelength computation: estimates via Arc-2D wavelets*

Figure 7(*a*,*b*) shows the computed IGW horizontal wavelength, λ_H, for all five simulations. As indicated in appendix A, the evolution of the IGW horizontal wavelength is computed on the particular xy sampling plane at a discrete number of transverse sampling locations, positioned within streamwise-aligned interrogation

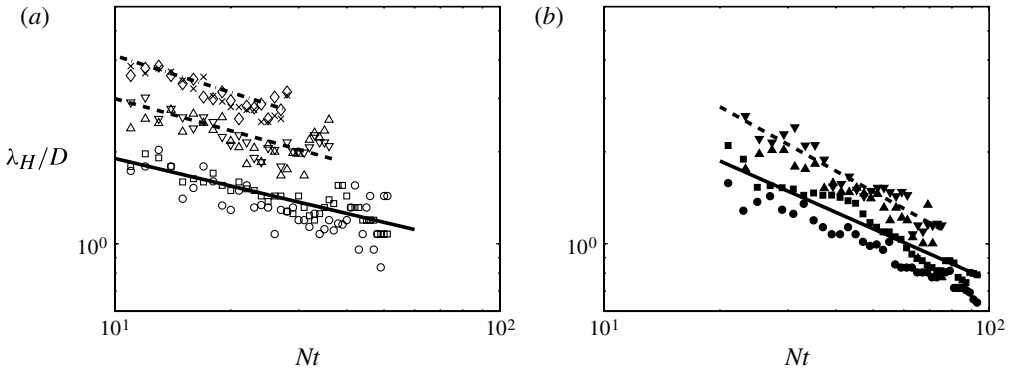

FIGURE 7. The evolution of the normalized horizontal wavelength obtained from the Arc wavelet transform of the horizontal divergence field on the xy sampling planes. Lines are band-averaged power-law fits where solid lines are for $Fr = 4$, dashed lines for $Fr = 16$ and dash-dotted lines for $Fr = 64$ simulations. (a) Symbols for (R5F4; $y/D = 1.5, 2.5$) are ($\circ$, $\square$), for (R5F16; $y/D = 1.5, 2.5$) are ($\triangle$, $\triangledown$) and for (R5F64; $y/D = 2.5, 4.5$) are ($+$, $\diamond$). (b) Symbols for (R100F4; $y/D = 1.5, 2.5$) are ($\bullet$, $\blacksquare$) and for (R100F16; $y/D = 1.5, 2.5$) are ($\blacktriangle$, $\blacktriangledown$).

strips. Nonetheless, for the sake of clarity, we show data from only two spanwise sampling locations.

Visualization (not shown) of the first arrival of measurable wave activity on the analysis plane shows a weak, spatially incoherent field with an estimated wavelength that changes slightly over a short period of time, of a duration of 5 to 10 buoyancy units, at the lower and higher Re, respectively. Since the estimated wavelengths in this stage are very likely to be an artefact of wavelet analysis applied to a weak incoherent signal propagating through the measurement plane, we elect to not plot λ_H during this initial period.

Following the above initial phase, the waves on the analysis plane become more coherent, appearing to have well-defined primary wavelengths. The initially sampled values of λ_H increase with Fr in accordance with the visualizations of the previous section. The computed wavelengths transition into a regime where they decrease at a uniform rate which is primarily dependent on Re and a lot less on Fr. Figure 7(b) also shows more spanwise variability of the computed wavelength at high Re relative to the low-Re cases (figure 7a).

Least-square power-law fits to the λ_H time series, averaged across all spanwise sampling locations within the transverse interrogation strips, are shown for all simulations in figure 7(a,b) as solid lines. The power law exponents are mainly Re-dependent, lying in the range $[-0.39, -0.3]$ for $Re = 5 \times 10^3$ and $[-0.7, -0.56]$ for $Re = 10^5$. At a given Re, the absolute value of the power law exponent weakly increases with Fr.

The weaker decrease rates we observe may be contrasted with the $1/Nt$ power law proposed by BCH and the large scatter of their data around the corresponding least-squares fit. However, a one-to-one comparison between both datasets may not be possible or even justifiable as details of the wave sampling and wavelength estimation algorithm were not given in BCH. Further discussion is deferred to § 6.2.

According to figure 7(a,b), the horizontal wavelength increases with increasing Fr. Initially, the high-Re horizontal wavelengths are comparable to their low-Re

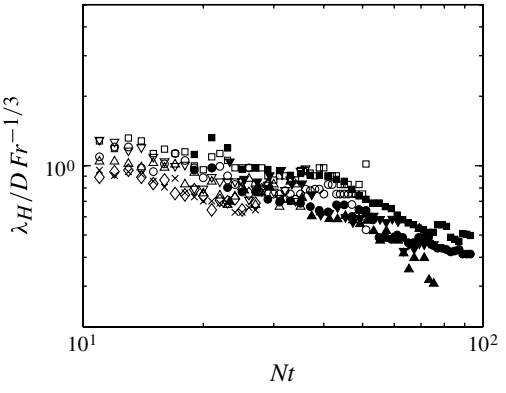

FIGURE 8. *Fr* scaling of the normalized horizontal wavelength obtained from the Arc wavelet transform of the horizontal divergence field in all five simulations. Symbols are the same as in figure 7.

counterparts. However, as the NEQ regime advances beyond $Nt = 30$, by virtue of the associated faster decrease rates, the high-*Re* values of λ_H become smaller by a factor of 1.5–2.

We now seek an *Fr* scaling that efficiently collapses the λ_H time series. A close examination of figure 7(*a*,*b*) shows that, for each (*Re*, *Fr*) pair, the first sampled value of λ_H on the observation plane is a factor of 2.5–3 larger than the near-constant mean wake half-height, L_V, observed by DSD during NEQ regime. Therefore, it appears that L_V may set the value of λ_H that is first observed at the *xy*-analysis plane and may also provide the desired *Fr* scaling.

Now, for a sphere wake whose mean profile does establish a self-similar evolution during the 3D regime, L_V is expected to scale as $Fr^{1/3}$ (Meunier, Diamessis & Spedding 2006). Taking into account the slightly faster rates of decrease at the higher *Re*, the application of this scaling to the λ_H time series appears to reasonably collapse them across all simulations (figure 8) in a manner similar to what was observed for the equivalent laboratory results of Spedding *et al.* (2000) who used similar arguments to Meunier *et al.*

Figure 8 also shows that the *Re*-dependence of the radiated IGW horizontal wavelengths is weak, with the primary difference being the faster rate of decrease of λ_H. This observation provides additional support to the suggestion that the IGWs first radiated by the wake, early in the NEQ regime, are generated by large-scale motions whose size is independent of *Re*.

Finally, note that throughout the entire duration of both high-*Re* simulations, λ_H is between a factor of five and eight larger than the diameter of the secondary K–H billows observed in DSD. This observation suggests that the IGWs do not directly originate from individual billows (see § 6.1 for further discussion).

5.2.2. *Horizontal wavelength computation via Morlet2D wavelets*

Close examination of figures 3–5 indicates that the orientation of the dominant wavenumber vectors of individual wave-packets does vary over space and time. Collectively, nonetheless, the wavenumber vectors tend to concentrate along a prevalent direction with slight deviations therefrom. The angle associated with the above preferred direction, hereafter called the resonant azimuthal angle, is not known *ab initio*. Details of the statistical procedure for its computation are outlined in

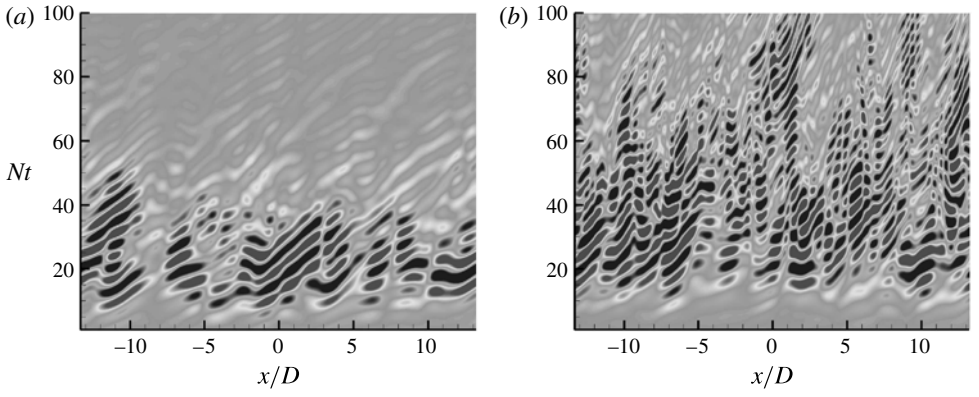

FIGURE 9. Streamwise distance–time (x–t) diagram of the normalized horizontal divergence field Δ_z/N for: (a) R5F4 at $y/D = 1.5, z/D = 1.5$ with minimum/maximum colourbar range $[-0.025,\ 0.025]$; (b) R100F4 at $y/D = 1.5, z/D = 1.5$ with minimum/maximum colourbar range $[-0.05, 0.05]$.

appendix B. On the particular xy-plane under examination, and at all spanwise sampling locations, the IGW field is interrogated with the Morlet2D wavelet transform at successive angles optimally spaced apart by 5° within the range $[0, \pm 90°]$. A search and averaging procedure (see appendix B) yields the optimum Morlet2D interrogation angle representing the direction along which the bulk of the wave field is oriented on the xy-plane at hand.

For all the reported simulations, the resonant azimuthal angle lies in the range $[56°, 60°]$ with no systematic dependence on either Re or Fr. Once the resonant azimuthal angle is estimated, the corresponding wavelet modulus cube from the application of the Morlet2D wavelet may be probed to obtain an alternative estimate of the IGW-field horizontal wavelength. The estimated power-law fits are in close agreement with those obtained from the Arc wavelet (for more detail see Abdilghanie 2010) which confirms the reliability and accuracy of the two types of wavelets and their suitability for the current application.

5.2.3. *Phase-line tilt angle*

Figures 9(a) and 9(b) show representative space–time (x–t) diagrams extracted at $(y/D, z/D) = (1.5, 1.5)$ for R5F4 and R100F4, respectively. Examination of low-Re data (figure 9a) at a particular x-location typically suggests a near-constant wave period. In contrast, in the high-Re data (figure 9b) there is more variability in the wave period over time, which tends to decrease as time advances.

In all five simulations, x–t diagrams are extracted at multiple spanwise locations located within the strips of significant wave activity (see appendix A) on the corresponding xy analysis plane. Analysis of these diagrams enables an accurate estimate of the frequency of the wake-radiated IGW field at a particular y/D-offset.

From each x–t diagram, twenty-one time series are extracted, at equally spaced locations within the interval $x/D \in [-10, 10]$. One-dimensional wavelet transforms of these time series are computed using the one-dimensional complex Morlet wavelet. The modulus of the corresponding CWT is a function of time and frequency.

For a particular wavelet-transformed time series, we conduct a one-dimensional search along the frequency axis at a given value of Nt to identify the frequency that maximizes the modulus of the transform, which is regarded as the resonant

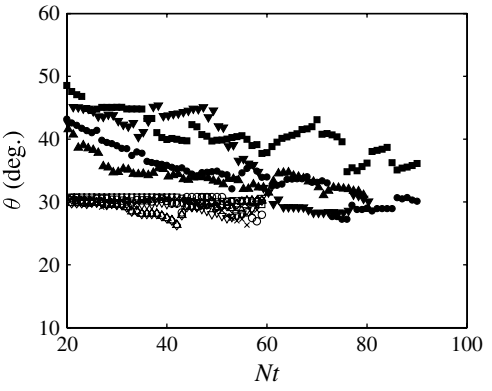

FIGURE 10. Evolution of the phase-line-tilt/polar angle obtained from the one-dimensional wavelet transforms. Symbols are the same as in figure 7.

frequency. Now, across the wavelet transforms for all time series, at a given Nt, the resonant frequencies are conditionally averaged. The conditional average retains only frequencies with a corresponding transform modulus value above 50 % of the global maximum across all time series. The frequencies are finally mapped onto equivalent phase-line tilt angles θ through the IGW dispersion relation.

A better understanding of the spanwise dependence of the spanwise variability of the phase-line tilt angle, θ, of the emitted IGW field may be gained by examining figure 10 which shows the evolution of θ at two representative spanwise locations for each of the five simulations considered here. The evolution of θ (and associated frequency value for a particular simulation) is consistent with the qualitative features found in figure 9(*a*,*b*). The observed values lie in the range $\theta \in [26°, 50°]$, which was observed in previous studies of IGWs generated in a well-mixed layer adjacent to a stable stratification (Sutherland & Linden 1998; Dohan & Sutherland 2003, 2005; Aguilar *et al.* 2006; Taylor & Sarkar 2007; Munroe & Sutherland 2008; Pham *et al.* 2009).

In figure 10, at low Re, the phase-line tilt angles for all three Fr values is strongly concentrated around 31°. Some weak departure to values no lower than $\theta = 26°$ occurs at later times when wave radiation has significantly diminished. The value of $\theta = 31°$ is close to 35°, the angle that maximizes the group velocity of the waves according to linear theory (Sutherland 2010). Accordingly, waves propagating at such an angle will experience the minimum viscous decay.

In the same figure, at high Re, the earliest observations of phase-line tilt angles, at $Nt = 20$, lie within the range [40°, 50°]; the IGW energy propagates at angles that are closer to the horizontal. Similar to the wavelengths, the computed phase-line-tilt angles show pronounced random spanwise variability relative to those at low Re. Now, the phase-line-tilt angles, especially around the time of maximum wave activity, are close to 45°, the value which maximizes the momentum extraction from the wake shear profile (Sutherland 2010). Nevertheless, at later times, the high-Re time series of θ converge to values close to those of their low-Re counterparts.

5.3. *Viscous effects in the propagation of radiated IGWs*

It is of interest to assess the role of viscosity in the selection of particular frequency subranges by the propagating IGW. We propose to track the distribution of resonant

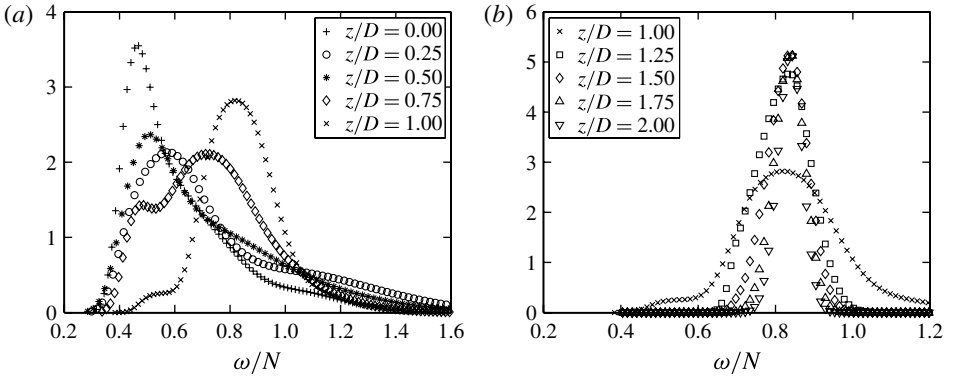

FIGURE 11. Computed p.d.f.s of resonant frequencies obtained from CWT of $(x–t)$ diagrams of the normalized horizontal divergence field Δ_z/N for R5F4 at $y/D = 1.5$, $z/D = 1.5$: (a) $z/D \in [0, 1]$, (b) $z/D \in [1, 2]$.

frequencies with height starting at the wake core ($z/D = 0$) and progressively monitoring any changes in this distribution with height. The lateral offset we choose to report representative results at is such that we begin at the wake centreline and transition into a region dominated by wake-radiated IGWs as we move upward. At progressively increasing vertical offsets with respect to the wake centreline, spaced apart equally by $\Delta z/D = 0.25$, we first extract $x–t$ diagrams similar to those in figure 9(a,b). We then analyse the time series extracted at a given streamwise location and extract the resonant frequencies, as described in § 5.2.3. We ultimately obtain 'an ensemble of resonant frequencies' for a given $x–t$ diagram at a particular height and spanwise offset.

The frequency content inside the turbulent region includes both non-propagating ($\omega/N > 1$) and propagating modes ($\omega/N < 1$). Conditionally averaging the frequency content therein, as currently done with the pure wave field on the vertically offset analysis planes, impedes making such a distinction. A more suitable approach is to approximate the resonant frequencies at a given height and spanwise offset as a continuous random variable in the frequency space. It is then possible to construct a histogram from the ensemble of resonant frequencies obtained from the time series extracted at the different streamwise sampling positions. Finally, to facilitate the comparison of the distributions at different heights, we estimate the shape of the associated probability density function (p.d.f.) using a normal smoothing kernel function (Bowman & Azzalini 1997).

Figure 11(a,b) shows the p.d.f.s at progressively increasing heights from the wake centreline for case R5F4, which is typical of all Re simulations considered here. For this value of Fr, following the wake half-height estimates for the NEQ regime of DSD, the turbulent region is concentrated within $0 \leqslant z/D \leqslant 0.5$. All the p.d.f.s of resonant frequencies sampled inside the turbulent region peak at a characteristic frequency of $\omega/N \approx 0.5 \pm 0.1$ independent of Reynolds and Froude numbers. This frequency is presumably associated with a vertical oscillation of the wake since it is consistently observed within its core. It is also intermittently observed in the wavelet analysis of time series sampled in the immediate vicinity of the edge of the turbulent region, in the form of the leftmost of two peaks of the p.d.f.s computed $z/D = 0.75$. What is exactly the origin of this oscillation remains to be determined. It may potentially be linked to slow vertical oscillations of the pancake vortices emerging towards the

end of the NEQ regime (Geoffrey Spedding, personal communication). Note that the energy density associated with the collapse of a well-mixed region in the experiments of Wu (1969) was found to peak around $\omega/N \approx 0.8$. However, any connection of Wu's finding with those reported here is at best tenuous since the turbulent wake does not undergo a similar collapse process.

Figure 11(*a*) shows that all the p.d.f.s up to $z/D = 0.5$ have a single peak and are skewed to the right, towards $\omega/N > 1$, with a visibly long tail. In all the simulations considered here (not shown), the right tail of all computed p.d.f.s for $\omega/N > 1$ inside the core converges to zero with some intermittent oscillations associated with low probability values.

In figure 11(*a*), a transition from a unimodal to a bimodal p.d.f. distribution subsequently occurs at $z/D = 0.75$, which corresponds to the edge of the wake core. This transition is associated with intermittent wake oscillations at the previously identified lower frequency peak of $\omega/N \approx 0.5 \pm 0.1$ and IGW emission at a higher frequency peak. This higher peak shifts to even higher values over a very short vertical distance, a possible outcome of highly nonlinear processes around the intermittent edge of the turbulent wake, converging to $\omega/N \approx 0.85$. At higher vertical offsets (figure 11*b*), the low-frequency peak vanishes and the p.d.f.s show strong rates of decay for frequencies on each side of the now dominant higher-frequency peak. For $z/D = 1.25$ and above, a narrow spectrum strongly peaking only at $\omega/N \approx 0.85$ is observed with this peak frequency corresponding to a propagation angle of 31°.

The continuous narrowing with height of the computed p.d.f.s around the higher-frequency peak can be attributed to the rapid viscous decay of the low- and high-frequency components of the radiated IGW field, in agreement with the fundamental mechanism underlying the viscous decay model of Taylor & Sarkar (2007). Nonetheless, the particular formulation of the viscous decay model considered by Taylor & Sarkar is not directly applicable to the wake-radiated IGW field considered here because the model relies on statistical stationarity and linearity of the underlying signal. The first condition is violated on account of the decaying turbulent source as opposed to the forced turbulent Ekman layer in Taylor & Sarkar (2007) that emits waves in a statistically stationary manner. In addition, the viscous decay model propagates an initial wave frequency spectrum from a prescribed spatial origin into the ambient fluid. Taylor & Sarkar select as a spatial origin a location where the IGW energy flux peaks and it is expected that most of the waves have been generated below this level. In the case of the wake, the most obvious choice of the spatial origin would be the edge of the turbulent wake. However, the rapid transition from a unimodal to a bimodal and back to a unimodal, though of a different peak frequency, structure of p.d.f.s in the vicinity of the wake edge, around $z/D = 0.75$, in figure 11(*a*,*b*) suggests that intermittent wave–turbulence interaction and other nonlinear processes are responsible for this rapid change in wave properties with vertical offset from the wake core. As a result, the second condition of applicability of the viscous decay model is also violated around the edge of the turbulent wake.

Note that application of the linear viscous decay model to fields with moderate to strong nonlinearity, namely higher Reynolds-number Ekman layers, has already been shown by Taylor & Sarkar (2008) to cause non-negligible errors in its predictions, namely an overestimation of the amplitude of high-frequency content of the wave spectrum. Additionally, the wave energy spectrum around the edge of the Ekman layer in Taylor & Sarkar (2007) is a lot broader than that in the wake edge and no rapid change of wave properties with height is reported in the former case. It appears that the localization of the turbulent wake in the spanwise direction in our simulation, as

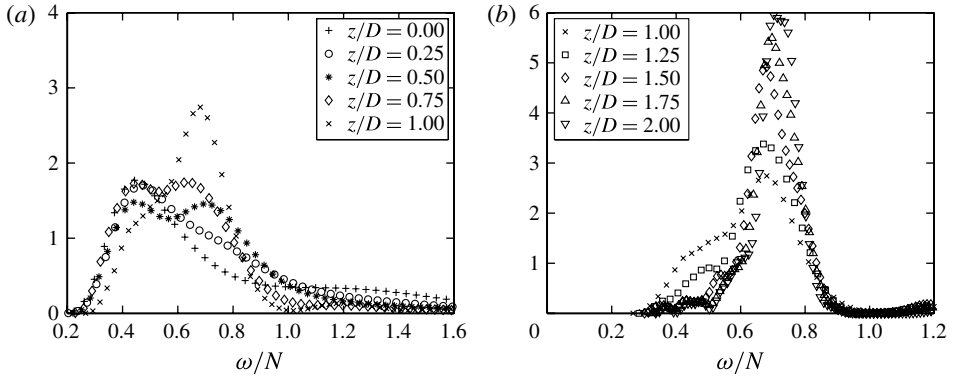

FIGURE 12. Computed p.d.f.s of resonant frequencies obtained from CWT of $(x–t)$ diagrams of the normalized horizontal divergence field Δ_z/N for R100F4 at $y/D = 1.5$, $z/D = 1.5$: (a) $z/D \in [0, 1]$; (b) $z/D \in [1, 2]$.

opposed to the Ekman layer that is statistically homogeneous in both the streamwise and spanwise directions, is responsible for the drastically different wave behaviour near the edge of the turbulent source. Nevertheless, the model prediction of rapid decay of the fast and slow frequency components with height appears to be generally supported by our low-*Re* simulation results.

However, the exact viscous time scale, or decay rate, of the wake-emitted IGWs is not straightforward to estimate since it requires an unambiguous estimate of the horizontal wavelength of the energetic wave-packets at the above spatial origin. Applying the two-dimensional CWT to the horizontal divergence field on xy planes close to the edge of the wake will not yield any reliable results since such planes are characterized by the coexistence of turbulence and waves. Since the current mother wavelets are optimized for wave fields, it is difficult (if not impossible) to coherently interpret the results of the resulting transform. In addition, there is no equivalent criterion for the two-dimensional CWT transform similar to $\omega/N > 1$ in frequency space which can separate propagating and non-propagating components, as done in the Fourier power spectra of Taylor & Sarkar (2007).

The corresponding p.d.f.s for case R100F4 (figure 12*a*,*b*) show a significantly different behaviour of the radiated IGW field outside the turbulent region from that observed for their low-*Re* counterparts. The transition from a bimodal to a unimodal p.d.f., with a high-frequency peak characteristic of a pure IGW field is again observed at the wake edge ($z/D = 0.5$ and 0.75). However, the p.d.f. at progressively higher vertical offsets does not display a strong decay of the frequency content on each side of the dominant frequency peak, as seen with the lower-*Re* data. Figure 12(*b*) actually shows a very weak change in the shape of the p.d.f. throughout the interval $1 \leqslant z/D \leqslant 2$, indicating that IGWs are subject to a much weaker influence of viscosity.

Finally, the prevalent frequencies at $z/D \geqslant 1$ for all simulations are consistent with the phase-line-tilt angles of figure 10. In all p.d.f.s computed for the low-Reynolds-number simulations, the frequency interval centred around the peak frequency and extending to half that value to the left and right of the peak, corresponds to a phase-line tilt angle of $\theta \in [26°, 31°]$. The higher Reynolds-number angles span a much wider $\theta \in [36°, 55°]$ range corresponding to a lower-frequency peak as is obvious in figure 12(*b*).

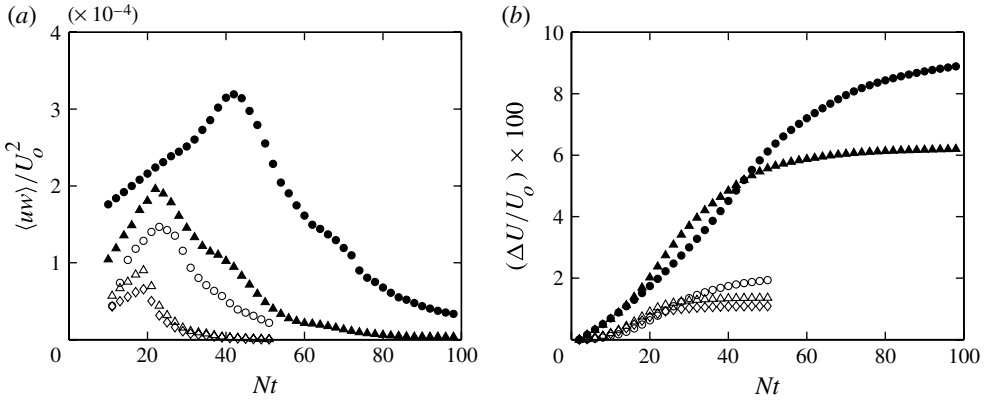

FIGURE 13. Evolution of the band-averaged wave momentum flux $\langle uw \rangle$. Averaging is performed over the full length of the computational domain and over a spanwise interval, symmetrically positioned around the wake centreline, with limits corresponding to the outer limits of the interrogation strips defined in appendix A. (*a*) Instantaneous value. (*b*) Cumulative drag. For both (*a*,*b*), U_o is the mean wake centreline velocity at $Nt = 2$. ○, R5F4; △, R5F16; ◇, R5F64; ●, R100F4; ▲, R100F16.

5.4. *Wave-driven momentum flux*

The vertical flux of horizontal momentum $\langle uw \rangle$ computed on the corresponding xy analysis planes is shown for each of the five simulations in figure 13(*a*). The spatial averaging, denoted by brackets, is performed over the full length of the computational domain for $x/D \in [-L_x/2D, L_x/2D]$ and over a limited interval in the spanwise direction for $y/D \in [-a/D, a/D]$ for which significant wave motion is observed. Note that a is case-dependent and corresponds to the outter edge of the interrogation strips defined in appendix A.

The momentum flux is normalized by U_o^2, an approximate measure of the momentum of the mean wake profile. U_o is the mean wake centreline velocity at the beginning of the NEQ regime assumed to be $Nt = 2$ (DSD; Spedding 1997). At low Re, the $Fr = 4$ wake undergoes the strongest extraction of momentum by the radiated IGW field. Between cases R5F16 and R5F64, the evolution of the IGW-driven momentum flux is very similar, although the peak value is a factor of two weaker and occurs a little earlier than in R5F4 case.

As shown in figure 10 and further supported by the analysis of § 5.3, high-Re wakes emit IGWs at angles where viscosity has a weaker impact on wave propagation. Moreover, according to linear theory, at such angles, momentum extraction from the IGW-generating mean wake flow is optimized. The high-Re results of figure 13(*a*) provide further support for such a claim. In particular, at a given Fr, the value of the peak momentum flux increases by a factor of two with respect to its low-Re counterpart. This peak value occurs somewhat earlier for R100F16 than for R100F4: at $Nt = 20$ versus $Nt = 40$.

Note that the vertical Reynolds stress at the planes of maximum vertical shear inside the wake, where the secondary turbulent events are concentrated, has been found to peak for runs R100F4 and R100F16 at times ∼5–10 buoyancy units before the observation of peak wave-driven momentum flux in figure 13(*a*) (see Diamessis 2010, for preliminary results on the former). It is at these earlier times, that the first well-recognizable and most potent secondary K–H instabilities appear in the horizontal

vorticity field, establishing significant vertical transport corresponding to vertical eddy viscosities that are five times as large as their molecular counterpart. These vertical eddy viscosities are likely to become even larger at higher Re, given the Re/Fr^2 scaling observed by DSD for buoyancy-driven shear which drives the secondary K–H instabilities. Nonetheless, the underlying cause of the occurrence of maximum vertical transport of momentum by secondary turbulence and radiated IGWs at comparable times remains unclear and is a topic of future investigation.

Most importantly, due to prolonged IGW radiation, driven by the secondary instabilities and turbulence inside the wake core, significant values of the wave-driven vertical momentum flux persist for as late as the end of the simulation for $Fr = 4$ and up to $Nt \approx 60$ for $Fr = 16$. This observation motivates the hypothesis that, with increasing Re, the mean velocity profile of a stratified turbulent wake can lose a non-negligible portion of its initial momentum into emitted IGWs.

The above hypothesis may be quantitatively explored by following the procedure used by Sutherland & Linden (1998). Specifically, one integrates the vertical flux of horizontal momentum in time, under the assumption that this momentum is extracted from a turbulent source concentrated over a characteristic vertical length scale of the mean/background velocity profile which sustains the turbulence. In this case, the appropriate length scale is the wake half-height, L_V, at the onset of the NEQ regime, which remains nearly constant throughout the NEQ regime (DSD; Spedding 2002). The relative reduction of the mean velocity profile, a measure of the wave-induced drag, is then given by

$$\frac{\Delta U}{U_o} = \frac{2}{U_o L_V} \int_{Nt=2}^{Nt_f} \langle uw \rangle \, \mathrm{d}t. \tag{5.3}$$

The factor of two accounts for the momentum extracted by the sum of the upward and downward propagating wave fields.

The evolution of the wave-induced drag is shown in figure 13(*b*). At a given Fr, the high-Re wake undergoes a reduction in the strength of its mean velocity profile that is nearly a factor of four higher than that of its low-Re counterpart. Note that at $Re = 5 \times 10^3$, the two higher-Fr curves are barely distinguishable. Further work is needed to determine whether such an observation indicates the possible existence of an Re-dependent upper bound of Fr, above which the mean momentum extracted by the radiated IGW field reaches a constant value. Our low-Re simulations have a maximum cumulative loss of momentum that is equal to 2 %, 1.4 % and 1 % of its initial value for $Fr = 4$, 16 and 64, respectively. The corresponding values for the high-Re runs are 8.9 % and 6.2 %.

6. Discussion

6.1. *Length scales of IGWs and turbulence*

Visual inspection of isopycnal contour plots (not shown here) indicates that the largest-scale turbulent overturning motions during the early stages of the NEQ regime have a vertical scale proportional to the full vertical extent of the wake. Therefore, since the IGWs arriving first at the xy analysis plane have a wavelength equal to 2.5 to 3 times the wake half-height L_V (see § 5.2.1), this initial wavelength is set by the above large-scale overturns.

In § 5.2.1, the initial IGW horizontal wavelength, λ_H, is found to be equal to a small multiple of the mean wake half-height, L_V. In addition, the λ_H time series collapse across all cases when an $Fr^{1/3}$ scaling is used. Recall that Gibson (1980) proposed that

the IGWs first emitted by a localized turbulent event embedded in a linear stratification have a wavelength equal to the Ozmidov scale, L_O, at the onset of buoyancy control (see § 1.2.3). Since we are using an implicit LES approach and a reliable estimate of the turbulent kinetic energy dissipation rate is not possible (see DSD for more details), we are unable to provide a corresponding reliable estimate of L_O throughout the entire wake evolution. Nonetheless, we seek to, at least indirectly, assess Gibson's claim by establishing a connection between L_O and L_V.

The Ozmidov scale of a stratified turbulent event, as defined in (1.1), represents the largest-scale vertical motion capable of generating density overturning (Ozmidov 1965; Dougherty 1961; Smyth & Moum 2000). At the onset of the NEQ regime, at $Nt \approx 2$, visual examination of the isopycnal fields across all simulations (not shown) shows overturning motions spanning a significant fraction of the vertical extent of the wake. As buoyancy indeed seizes control of the largest scales of turbulent motion at this time, it is reasonable to assume that the vertical scale of these overturns provides a measure for L_O at this time. As a result, it is very likely that $L_O = \alpha L_V$ at the beginning of the NEQ regime, with $\alpha \in [2, 4]$.

Moreover, Spedding (2002) proposed an $Fr^{1/3}$ scaling for L_O at the onset of the NEQ regime by assuming a self-similar power-law behaviour for the integral scale and characteristic velocity of the three-dimensional turbulence prior to the onset of this regime. This scaling was independently confirmed by Spedding's experimental data which indicated an $Fr^{-7/3}$ scaling for the measured kinetic energy dissipation rate. The above observation-based estimate of L_O and associated connection with L_V at the onset of the NEQ regime and the existence of an$Fr^{1/3}$ scaling for both L_O and L_V and also λ_H do lend support to Gibson's claim. Additional support for this claim was provided by the recent experiments of Clarke & Sutherland (2010) who found that the Ozmidov scale of the turbulence in the vicinity of an oscillating cylinder, and not the cylinder diameter, is what sets the wavelength of the radiated IGWs.

In the high-Re simulations considered here, turbulence persists throughout the entire NEQ regime. The question thus arises of whether the Ozmidov scale of the secondary events (occurring long after the original three-dimensional turbulence has been overcome at all scales by buoyancy) sets the radiated IGW wavelength observed at later times during the NEQ regime. However, unlike the early-time three-dimensional turbulence that spans the large fraction of the wake's full vertical extent, the secondary turbulence of the NEQ regime operates within the vertical confines of thin horizontal vorticity layers (DSD; Brethouwer *et al.* 2007), with each secondary turbulent event having its own local Ozmidov scale (Linborg 2006). An estimate of L_O during the NEQ regime at high Re may be obtained by examining stream-depth and span-depth transects of the spanwise vorticity and isopycnal fields at the corresponding times (not shown here) and measuring the billow diameter. In such transects, the largest overturning length scale is typically the diameter of the secondary K–H billows, which can then serve as an approximate measure of the desired value of L_O (or upper bound thereof, depending on the degree of buoyancy control within the billow under consideration). As discussed in § 5.2.1, the computed IGW horizontal wavelengths are always a factor of 5 to 8 larger than the diameter of the K–H billows reported by DSD. Therefore, a more complex mechanism is operative at these later times at higher Re, whereby the secondary turbulent flow structures displace the isopycnal surfaces and the observed values of λ_H come into being.

Finally, note that Taylor & Sarkar (2007) were not able to identify a correlation between λ_H and L_O for a turbulent source operating in a well-mixed background. However, their observation is most likely linked to the considerably different turbulent

dynamics of their configuration compared to those of a wake embedded in a linear stratification.

6.2. *Evolution of IGW wavelengths*

Despite the link between the wavelength of the IGWs first emitted by the wake and the vertical wake half-height at the beginning of the NEQ regime, questions remain as to what mechanism is responsible for the observed decrease over time of the computed wavelength. As proposed by BCH, IGW dispersion is the primary candidate here since long-wavelength components reach the analysis plane faster than waves with smaller wavelength. However, we find λ_H to decrease with power laws that are significantly slower than the $1/Nt$ decrease rate which is characteristic of linear dispersion of waves emitted by an isolated wave source.

Our estimated p.d.f.s of resonant frequencies in figures 11(*a*,*b*) and 12(*a*,*b*) also show a very rapid change in wave properties near the edge of the turbulent wake indicating that nonlinear processes including wave–wave interactions, interference of waves emitted from different locations within the wake, and wave–turbulence interactions are indeed important. Note that wave interference might be the cause of observed gradual loss of wavepacket coherence, especially at high Re (see figures 4 and 5) where the density of waves and accordingly the number of effective local sources of IGWs within the wake noticeably increases.

At higher values of Re and Fr, since the wave steepness (and also the displacement amplitude; see § 5.1) increase significantly, nonlinear dispersion might act to add significant high-order corrections to wave frequency (Sutherland 2010). Finally, at high Re, the underlying physics becomes even more complicated, as the continuous IGW radiation is linked to different coherent vortical structures inside the wake such as successive secondary K–H instabilities and turbulence occurring throughout the NEQ regime.

Further analysis, beyond the scope of this paper, would be needed to determine the role of the various mechanisms discussed above in setting the decrease rate of the IGW wavelength. From the point of view of developing more realistic reduced models of a stratified wake, the commonly employed models using impulsive sinks and source could be augmented to contain multiple such sources of IGWs that interact nonlinearly, especially in the vicinity of the wake boundary, with nonlinear dispersion possibly playing an important role in IGW propagation.

6.3. *IGW emission and momentum extraction at high Reynolds number*

The azimuthal angle of the wake-radiated IGWs is concentrated around a mean direction of approximately 60°, independent of both Re and Fr. In contrast, the IGW phase-line-tilt angle with respect to the vertical does show a visible Re dependence (figure 10). In all low-Re simulations, the angles were constant over time and equal to $\theta = 31°$, a value which is close to the 35° value that maximizes the vertical group velocity of the wave field (Sutherland 2010). Further evidence of the dominant effect of viscosity at low Reynolds number is established through the gradual narrowing of the shape of resonant-frequency p.d.f.s with height along their propagation path outside the turbulent core, in agreement with the fast decay rate of low- and high-frequency components suggested by the viscous decay model of Taylor & Sarkar (2007). Waves with such a phase-line tilt angle are thus subject to minimum viscous decay which suggests that, at these low Re, IGW radiation is a viscously-dominated process, independent of the strength of the stratification.

However, at high *Re*, the dynamics of the wake core and wave propagation are subject to a much weaker influence of viscosity, thus allowing the resulting secondary instabilities and turbulence (DSD) within the wake to sustain IGW radiation at a wider range of propagation angles. Taking into account any variability observed in the spanwise direction, the most intense wave emission now shifts towards phase-line tilt angles of $\theta \approx 45^\circ$ for a significant part of the NEQ regime. However, towards the end of this regime, the phase-line tilt angles asymptote towards the corresponding low-*Re* angle, indicating that, given enough time, viscous effects do become important. Waves propagating at approximately 45° are associated with the maximum vertical flux of horizontal momentum (Sutherland 2010) away from the wake; the wake undergoes a non-negligible drag as indicated in figure 13(*b*). Consequently, whereas, at low *Re*, IGW emission has a negligible impact on the dynamics of the wake core, at high *Re*, especially at values of $O(10)$ or higher than those considered in this paper, the non-negligible wave drag it causes may considerably affect the wake dynamics.

It is interesting to note the propagation angle of $\theta \approx 45^\circ$ of emitted waves in the earlier part of the NEQ regime in our high-*Re* simulations and the prevalence of this same angle value in the wave field emitted by forced turbulent mixed regions. In the latter, Sutherland & Linden (1998) hypothesized that such an angle is the result of an equilibrium state of a highly nonlinear coupling between the emitted waves and the mixed region dynamics. The presumed coupling maximizes wave drag on the mean shear within the turbulent region while, at the same time, prevents wave radiation from continuously draining the shear of its energy. The observed continuous decrease of the wave emission angle over time in our high-*Re* simulations may be attributed to the drastically different manner in which buoyancy controls the dynamics of a decaying turbulent source in a stratified environment with respect to the dynamics of a well-mixed, forced turbulent source.

Insight into the coupling between the wake-radiated IGW field and the coherent vortical structures that generate it in a stratified fluid can be obtained by appealing to the theoretical model of Plougonven & Zeitlin (2002). Nonetheless, a degree of caution is warranted in this regard, as the above model is fully inviscid. The time at which unambiguously identifiable pancake vortices emerge in the wake core corresponds to the final stages of the NEQ regime, regardless of the wake *Re* (DSD). The bulk of IGW radiation has occurred prior to this point in time and is attributed to more complex flow structures (including secondary K–H instabilities and turbulence; see § 1.2.1). Moreover, these quasi-horizontal vortical motions have a horizontal Reynolds number (based on diameter and characteristic horizontal velocity) of $O(1)$ that, by virtue of viscosity, renders them robust to possible destabilization by IGW radiation, a phenomenon proposed by Plougoven & Zeitlin. Under more inviscid conditions, any destabilization of such vortices is also more likely to be caused by alternative mechanisms such as the zig-zag instability (Deloncle, Billant & Chomaz 2008).

Finally, a question that arises is whether, as *Re* is increased, there is an upper limit for the efficiency at which IGW radiation can extract momentum, from the wake core. Moreover, as proposed by DSD, the duration of the NEQ regime increases with *Re*. The previous question may thus be reformulated as to whether, at operationally and geophysically relevant *Re* of $O(10^8)$ to $O(10^{11})$ (Pao, Lai & Schemm 1982), IGW radiation depletes the wake of all its momentum and energy before viscous effects do (Gibson 1980).

Given that the K–H billows characteristic of the high-*Re* NEQ regime have a horizontal length scale (DSD) considerably smaller than the horizontal wavelength

of the wake-emitted IGWs (see § 5.2.1), these waves are apparently generated by larger scales of the turbulence inside the wake core; the K–H billows, nonetheless, should have a non-negligible role in the generation process. With respect to the sphere diameter D, as one increases Re, these scales become increasingly removed from the smaller scales of motion inside the wake which are directly impacted by viscosity. Given this reduced impact of viscosity, it is thus reasonable to assume that energy at these large-scales of the wake core is more readily available to be channelled to emitted IGWs than in the low-Re case. Moreover, one might perceive the radiation of IGWs as the dominant momentum/energy sink for the wake, as now buoyancy has dominated almost the entire range of scales inside the wake. However, a competing process at high Re is the Kolmogorov-like forward cascade of turbulent energy in the horizontal associated with the secondary instabilities and turbulence, as evidenced in the horizontal one-dimensional spectra with a broad inertial range (DSD; Riley & de Bruyn Kops 2003; Linborg 2006; Riley & Lindborg 2008) and the Kolmogorov scaling for the turbulent kinetic energy dissipation rate identified by (Brucker & Sarkar 2010). Additional simulations at even higher Re, which will become feasible once the appropriate computational resources become available, will allow us to further explore the above question on the relative strength of these two processes in depleting the mean wake flow of its momentum, and energy.

7. Concluding remarks

The near-field properties of the internal gravity wave (IGW) field emitted by a stratified turbulent wake with non-zero net momentum have been examined through fully nonlinear spectral multidomain-based numerical simulations. Instrumental in the analysis of the highly complex and spatially localized quasi-random wake-emitted IGW field is the use of the continuous wavelet transform (CWT) in one and two dimensions.

At higher Re, on account of the prolongation of the non-equilibrium (NEQ) regime in wake evolution through secondary Kelvin–Helmholtz instabilities and turbulence, IGW radiation persists much longer than at lower Re values typical of the laboratory, suggesting a possible change in IGW generation mechanism. A visible reduction in IGW horizontal wavelengths is observed at high Re. These wavelengths increase with increasing Fr. Furthermore, the phase-line tilt angles of IGWs with respect to the vertical are found to lie in a narrow range of values that is predominantly Re-dependent. At low Re, IGW emission is a viscously driven process, whereby waves are radiated by the wake core at 31° from the vertical, an angle that allows minimum viscous decay. The associated drag on the mean wake flow is negligible. At high Re, viscous effects are initially quite weaker, causing the radiated waves to propagate at angles within the range of $[40°, 55°]$ which induce a non-negligible drag on the mean wake flow. Subsequently, viscous effects seem to drive the angle towards its equivalent low-Re value. This particular result sets decaying stratified turbulent wakes apart from forced mixed turbulence where the higher wave propagation angles are consistently observed regardless of Re. Additional work is needed to explore Sutherland's hypothesis (Sutherland & Linden 1998) that nonlinear wave–mean flow interactions are the direct cause of the predominance of such higher angles in numerical and experimental observations. Although IGW radiation can become a significant sink of wake momentum and energy, further research is needed to ascertain whether there is an upper bound on the rate of wake momentum and energy loss to

emitted waves and how this rate compares to the turbulent kinetic energy dissipation rate inside the wake.

The quantification of the properties of the near-field wake-radiated IGWs enabled by this work provides insight that can contribute towards the refinement of existing reduced models of IGW radiation that are based on the superposition of impulsive mass sources and sinks (Voisin 1991, 1994). Critical to such a refinement effort is to take into account the significant reduction in decay rates of the IGW horizontal wavelengths and the continuous wave emission observed in the simulations. This continuous radiation may be contrasted to the pulse-like emission mechanism inherent in the above reduced models. In addition, the IGW fields generated in this study can serve as reliable initial conditions for computational fast-turnaround ray-tracing models (Broutman, Rottman & Eckert 2004).

Nevertheless, beyond the efforts presented here, significant additional work is needed. On one hand, there are numerous aspects of the physics of IGW generation by a high-Re localized turbulent source that need to be clarified. In this regard, an important unresolved question is to determine the exact differences in the dynamics of a turbulent source operating in either a stratified environment or in a well-mixed background lying above or below a stratified region. On the other hand, additional simulations with more powerful computational resources are needed in the future. Runs in taller and wider domains would allow us to study conditions more relevant to geophysical and naval applications; that is a wider range of Re and Fr (Pao *et al.* 1982; Spedding 1997). In the latter case, Fr may be as high as $O(500)$. The availability of such runs will enable further investigation into some of the issues and questions raised in this study. These include the existence of an optimum Fr (and possibly Re) value for maximizing momentum extraction by the waves, reliable scaling of the maximum displacement amplitude, and assessment of the potential for wave breaking both near and far from the wake boundary.

Additionally, a more detailed computation of the energy flux transported by the emitted waves is needed. Computing this flux and assessing its relative strength with respect to the turbulent kinetic energy dissipation rate and mixing induced within the wake would ideally require a highly costly DNS that would resolve the full range of scales within the wake core at high Re, namely the secondary turbulent events. Finally, an outstanding question of paramount importance lies in deciphering how exactly broadband turbulence embedded in a stably stratified background (and not neighbouring it while operating in a well-mixed region) generates IGWs and whether there is a particular coherent structure inside the wake core whose frequency or length scale can be linked to the frequency or the wavelength of the radiated IGWs, respectively.

Acknowledgements

We are thankful to Professor G. R. Spedding for guidance on the theory and use of the two-dimensional continuous wavelet transforms. We also thank Professor J. J. Riley for a number of insightful comments. Q. Zhou is thanked for generating the three-dimensional visualizations. We are grateful to three anonymous reviewers for their insightful commentary. Support through Office of Naval Research grant N00014-08-1-0235 administered by Dr R. Joslin is gratefully acknowledged. The second author also acknowledges the support of National Science Foundation CAREER award Grant OCE-0845558.

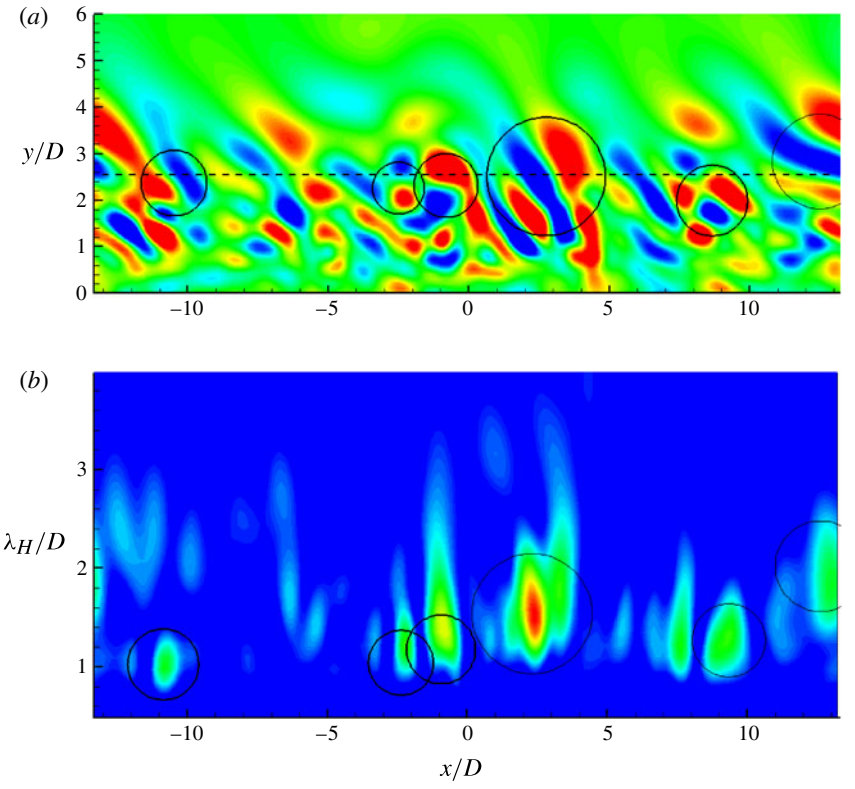

FIGURE 14. (*a*) Normalized horizontal divergence field on the left half of a horizontal *xy*-plane at $z/D = 1.5$ for R5F4 at $Nt = 30$. The minimum/maximum range for the colourbar is $[-0.04, 0.04]$. (*b*) Vertical transect at $y/D = 2.5$ of the corresponding wavelet transform modulus cube applied to the full *xy*-analysis plane. The spanwise offset at which the transect is performed is marked on (*a*) with a dashed horizontal line. The modulus of the transform is locally maximized at several downstream locations. The approximate influence band for each local peak is delineated with a circle. The wavelength of the corresponding IGW packet on (*a*) is given by the vertical coordinate of the centre of the influence band. The most coherent and most energetic wavepacket at $y/D = 2.5$ in (*a*) is centred around $x/D = 3$. Such a wavepacket leads to the strongest resonance in (*b*) which is observed at the same x/D location with influence band centred around $\lambda_H/D = 1.5$ which is the wavelength of the packet under consideration.

Appendix A. Horizontal wavelength computation: preliminaries

The specifics of two-dimensional wavelet analysis of the wake-radiated IGW field may be illustrated by considering an example vertically offset *xy* transect of the Δ_z/N field from run R5F4, specifically the one at $Nt = 30$ shown in figure 14(*a*). This snapshot is effectively the same as the $Fr = 4$, $Nt = 30$ snapshot in figure 3 but with only positive spanwise coordinate values shown and colour contours used to best illustrate the most energetic wave-packets. We first examine the application of the two-dimensional Arc wavelet transform to the horizontal divergence field data on this example *xy* transect. The resulting modulus transform data cube (the space-scale, (x, y, λ_H), domain) is scanned for resonance.

Figure 14(*b*) shows a vertical transect at $y/D = 2.5$ through the modulus transform data cube. Localized regions, called bands of influence, are immediately visible where

the modulus of the transform is maximized, as a result of resonance with wavepackets located at the same $(x/D, y/D)$ position. The centre of the vertical coordinate of the bands provides the associated spatial scale. The most prominent influence bands and their corresponding wave-packets are circled in the two panels of the figure. The area of a given band of influence is proportional to the wavelength; the greater the wavelength of the resonant wavepacket, the larger the area where the transform is maximized (Dallard & Spedding 1993; Spedding *et al.* 1993). The centres of the influence bands are concentrated around an average wavelength of $\lambda_H/D = 1.5$ with small deviations across all peaks (typically less than $0.5D$).

Taking into account the random-like nature and the dynamical evolution of the IGW-radiating turbulent wake source, it does not suffice to report wavelength values at a fixed location on the xy analysis plane as done in Gilreath & Brandt (1985) and apparently in BCH as well. Waves of a certain scale detected at this particular location may not be detected at the same location in different realizations of the flow with statistically identical, yet instantaneously different, initial conditions. To this end, and on account of the streamwise homogeneity of the wave source, the streamwise average of the resonant wavelengths is expected to be repeatable across different realizations of the flow and is thus the only reliable information to report.

Thus, the results we ultimately present are time series of the conditionally averaged wavelength at discrete values of y/D from the centreline (see figure 7*a*,*b*). These locations of spanwise offset are contained within pre-defined limits of y/D, as elaborated below. At the y/D offset at hand, the conditional averaging procedure consists of averaging the value of λ_H/D (referred to as the resonant wavelength) that maximizes the modulus of the wavelet transform at 21 equally spaced downstream x/D locations in the interval $x/D \in [-10, 10]$. At each x/D location, only wavelengths with a local peak of the transform modulus below 50 % of the global peak transform modulus are considered. The peak modulus is identified over all grid points in the full x/D interval at the particular spanwise offset.

The presence of a sufficiently large ensemble of wave-packets on either side of the wake centreline allows us to limit our averaging on one side of the wake and obtain sufficiently converged statistics. No further averaging at the symmetrically spanwise-offset position is needed.

The search for resonance in the spanwise direction on the xy-plane at hand is limited to streamwise-aligned interrogation strips where significant wave activity occurs throughout the entire simulation. To minimize the computational cost of the analysis and exclude statistically dependent data, we sample the transform modulus data at a discrete number of equally spaced y/D locations within these strips. Successive sampling locations are spaced apart by one sphere diameter, D. For case R5F4, the interrogation strip is limited within the spanwise interval $1.5 < y/D < 4.5$. The spanwise extent of the search strips is increased with Fr, and is set to $1.5 < y/D < 6.5$ and $1.5 < y/D < 8.5$, for R5F16 and R5F64, respectively, retaining the same spanwise offset between successive spanwise sampling locations. Given that the wave emission is prolonged at the higher Re and on account of the continued lateral wake growth, the spanwise extent of the above search strips is increased relative to the low-Re case. Specifically, strips spanning $1.5 < y/D < 6.5$ and $1.5 < y/D < 8.5$ are used for R100F4 and R100F16, respectively. To avoid edge effects, we discard the modulus data over a region of length approximately $3D$ near the left and right streamwise boundaries of the domain.

Appendix B. Resonant azimuthal angle and circular data statistics

This appendix outlines the technique used to compute the resonant azimuthal angle of the wake-radiated IGW field. At increments of $Nt = 1$, the horizontal divergence field on the xy-plane under consideration is transformed with the Morlet2D wavelet using selected *a priori*-prescribed interrogation angles in the interval $[0, \pm 90°]$. Successive interrogation angles are equally spaced apart by 5°. A smaller angle spacing is not only more costly, as more wavelet transforms are required, but is also found to not produce significantly different results between two successive angles. For each Nt value above, at a given y/D offset, the interrogation angles, ϕ_i, that resonate with the wave field by producing the maximum modulus of the wavelet transform are recorded at $N = 21$ equally spaced x/D locations within the interval $x/D \in [-10, 10]$.

The computed resonant angles across all locations and times do not vary significantly. Thus a single average angle, referred to as the resonant azimuthal angle, is ultimately reported, with the averaging performed over the range of ϕ_i given above. A standard circular data-averaging-technique (see Trauth 2010), is essential to avoid what is known as the wraparound effect at $\phi = 360°$. This effect incorrectly estimates the arithmetic average of the angles 6° and 354° as 180° and the standard deviation with respect to the mean as 246°. The appropriate average is defined as:

$$\overline{\phi} = \tan^{-1}(x_r/y_r), \tag{B 1}$$

where

$$x_r = \sum_{i=1}^{N} \sin(\phi_i), \tag{B 2}$$

and

$$y_r = \sum_{i=1}^{N} \cos(\phi_i). \tag{B 3}$$

A measure of the dispersion around the average angle is then given by the circular variance:

$$\sigma_o = 1 - \overline{R}, \tag{B 4}$$

where

$$\overline{R} = \left(\sqrt{x_r^2 + y_r^2}\right)/N. \tag{B 5}$$

The more concentrated the angles are around a single mean direction, corresponding to the resonant azimuthal angle, the smaller the value of the circular variance. In all the reported simulations, the mean directions of all resonance angles at all locations and times were in the range $[56°, 65°]$ with typical circular variance $\sigma_o \approx 0.03$ indicating very small departure from the mean direction. For a graphical illustration of the concentration of the angles around a single mean value, the interested reader is referred to the Rose diagrams in Abdilghanie (2010).

REFERENCES

ABDILGHANIE, A. M. 2010 A numerical investigation of turbulence-driven and forced generation of internal gravity waves in stratified mid-water. PhD thesis, Cornell University.

ADDISON, P. S. 2002 *The Illustrated Wavelet Transform Handbook*. Institute of Physics.

AGUILAR, D. A. & SUTHERLAND, B. R. 2006 Internal wave generation from rough topography. *Phys. Fluids* **18**, 066603.

AGUILAR, D. A., SUTHERLAND, B. R. & MURAKI, D. J. 2006 Laboratory generation of internal waves from sinusoidal topography. *Deep-Sea Res.* II **53** (1–2), 96–115.

BONNETON, P., CHOMAZ, J. M. & HOPFINGER, E. J. 1993 Internal waves produced by the turbulent wake of a sphere moving horizontally in a stratified fluid. *J. Fluid Mech.* **254**, 23–40.

BONNIER, M., BONNETON, P. & EIFF, O. 1998 Far-wake of a sphere in a stably stratified fluid: characterization of vortex structures. *Appl. Sci. Res.* **59**, 269–281.

BOWMAN, A. W. & AZZALINI, A. 1997 *Applied Smoothing Techniques for Data Analysis: The Kernel Approach with S-Plus Illustrations*, Oxford Statistical Science Series, vol. 18. Oxford University Press.

BRETHOUWER, G., BILLANT, P., LINDBORG, E. & CHOMAZ, J. M. 2007 Scaling analysis and simulation of strongly stratified turbulent flows. *J. Fluid Mech.* **585**, 343–368.

BROUTMAN, D., ROTTMAN, J. W. & ECKERT, S. D. 2004 Ray methods for internal waves in the atmosphere and ocean. *Annu. Rev. Fluid Mech.* **36**, 233–253.

BRUCKER, K. A. & SARKAR, S. 2010 A study of momentumless wakes in stratified fluids. *J. Fluid Mech.* **652**, 373–404.

CHASHECHKIN, Y. D. 1989 Hydrodynamics of a sphere in a stratified fluid. *Fluid Dyn.* **24** (1), 1–7.

CLARKE, H. A. & SUTHERLAND, B. R 2010 Generation, propagation, and breaking of an internal wave beam. *Phys. Fluids* **22**, 076601.

DALLARD, T. & SPEDDING, G. R. 1993 2-D wavelet transforms: generalisation of the Hardy space and application to experimental studies. *Eur. J. Mech. (*B/*Fluids)* **12** (1), 107–134.

DELONCLE, A., BILLANT, P. & CHOMAZ, J. M. 2008 Nonlinear evolution of the zigzag instability in stratified fluids: a shortcut on the route to dissipation. *J. Fluid Mech.* **599**, 229–239.

DIAMESSIS, P. J. 2010 Vertical transport in high Reynolds numbers stratified turbulent wakes. In *Sixth International Symposium on Environmental Hydraulics, Athens, Greece*.

DIAMESSIS, P. J., DOMARADZKI, J. A. & HESTHAVEN, J. S. 2005 A spectral multidomain penalty method model for the simulation of high Reynolds number localized stratified turbulence. *J. Comput. Phys.* **202**, 298–322.

DIAMESSIS, P. J., GURKA, R. & LIBERZON, A. 2010 Spatial characterization of vortical structures and internal waves in a stratified turbulent wake using proper orthogonal decomposition. *Phys. Fluids* **22**, 086601.

DIAMESSIS, P. J. & NOMURA, K. K. 2000 Interaction of vorticity, rate-of-strain and scalar gradient in stratified homogeneous sheared turbulence. *Phys. Fluids* **12**, 1166–1188.

DIAMESSIS, P. J., SPEDDING, G. R. & DOMARADZKI, A. J. 2011 Similarity scaling and vorticity structure in high Reynolds number stably stratified turbulent wakes. *J. Fluid Mech.* **671**, 52–95.

DOHAN, K. & SUTHERLAND, B. R. 2003 Internal waves generated from a turbulent mixed region. *Phys. Fluids* **15**, 488.

DOHAN, K. & SUTHERLAND, B. R. 2005 Numerical and laboratory generation of internal waves from turbulence. *Dyn. Atmos. Oceans* **40**, 43–56.

DOMMERMUTH, D. G., ROTTMAN, J. W., INNIS, G. E. & NOVIKOV, E. A. 2002 Numerical simulation of the wake of a towed sphere in a weakly stratified fluid. *J. Fluid Mech.* **473**, 83–101.

DOUGHERTY, J. P. 1961 The anisotropy of turbulence at the meteor level. *J. Atmos. Terr. Phys.* **21** (2–3), 210–213.

DRUZHININ, O. A. 2009 Generation of internal waves by a turbulent jet in a stratified fluid. *Fluid Dyn.* **44**, 213–223.

DURRAN, D. R. 1999 *Numerical Methods for Wave Equations in Geophysical Fluid Dynamics*. Springer.

GAYEN, B., TAYLOR, R. J. & SARKAR, S. 2010 Large eddy simulation of a stratified boundary layer under an oscillatory current. *J. Fluid Mech.* **643**, 233–266.

GIBSON, C. H. 1980 Fossil temperature, salinity and vorticity in the ocean. In *Marine Turbulence* (ed. J. C. T. Nihoul), pp. 221–258. Elsevier.

GILREATH, H. E. & BRANDT, A. 1985 Experiments on the generation of internal waves in a stratified fluid. *AIAA J.* **23**, 693–700.

GOURLAY, M. J., ARENDT, S. C., FRITTS, D. C. & WERNE, J. 2001 Numerical modelling of initially turbulent wakes with net momentum. *Phys. Fluids* **13**, 3783–3802.

HOPFINGER, E. J., FLOR, J. B., CHOMAZ, J. M. & BONNETON, P. 1991 Internal waves generated by a moving sphere and its wake in a stratified fluid. *Exp. Fluids* **11** (4), 255–261.

ISRAELI, M. & ORSZAG, S. A. 1981 Approximation of radiation boundary conditions. *J. Comput. Phys.* **41** (1), 115–135.

ITSWEIRE, E. C., KOSEFF, J. R., BRIGGS, D. A. & FERZIGER, J. H. 1993 Turbulence in stratified shear flows: implications for interpreting shear-induced mixing in the ocean. *J. Phys. Oceanogr.* **23**, 1508–1522.

KEELER, R. N., BONDUR, V. G. & GIBSON, C. H. 2005 Optical satellite imagery detection of internal wave effects from a submerged turbulent outfall in the stratified ocean. *Geophys. Res. Lett.* **32** (12), L12610.

KLEMP, J. B. & LILLY, D. K. 1978 Numerical simulation of hydrostatic mountain waves. *J. Atmos. Sci.* **35** (1), 78–107.

LIGHTHILL, J. 1978 *Waves in Fluids*. Cambridge University Press.

LIGHTHILL, M. J. 1952 On sound generated aerodynamically. I. General theory. *Proc. R. Soc. Lond.* A **211** (1107), 564–587.

LILLY, D. K. 1983 Stratified turbulence and the mesoscale variability of the atmosphere. *J. Atmos. Sci.* **40**, 749–761.

LINBORG, E. 2006 The energy cascade in a strongly stratified fluid. *J. Fluid Mech.* **550**, 207–242.

LINDEN, P. F. 1975 The deepening of a mixed layer in a stratified fluid. *J. Fluid Mech.* **71** (2), 385–405.

MENG, J. C. S. & ROTTMAN, J. W. 1988 Linear internal waves generated by density and velocity perturbations in a linearly stratified fluid. *J. Fluid Mech.* **186**, 419–444.

MEUNIER, P., DIAMESSIS, P. J. & SPEDDING, G. R. 2006 Self-preservation of stratified momentum wakes. *Phys. Fluids* **18**, 106601.

MILES, J. W. 1971 Internal waves generated by a horizontally moving source. *J. Geophys. Astrophys. Fluid Dyn.* **2** (1), 63–87.

MOUM, J. N., HEBERT, D., PAULSON, C. A. & CALDWELL, D. R. 1992 Turbulence and internal waves at the equator. Part I: Statistics from towed thermistors and a microstructure profiler. *J. Phys. Oceanogr.* **22** (11), 1330–1345.

MUNROE, J. R. & SUTHERLAND, B. R. 2008 Generation of internal waves by sheared turbulence: experiments. *Environ. Fluid Mech.* **8** (5), 527–534.

NAPPO, C. J. 2002 *An Introduction to Atmospheric Gravity Waves*. Academic.

ORSZAG, S. A. & PAO, Y. H. 1975 Numerical computation of turbulent shear flows. *Adv. Geophys.* **18** (1), 225–236.

OZMIDOV, R. V. 1965 On the turbulent exchange in a stably stratified ocean. *Izv. Acad. Sci. USSR, Atmos. Ocean. Phys.* **1**, 853–860.

PAO, H. P., LAI, R. Y. & SCHEMM, C. E. 1982 Vortex trails in stratified fluids. *Tech. Rep.* 3(1). Johns Hopkins Applied Physics Laboratory Technical Digest.

PEAT, K. S. & STEVENSON, T. N. 1975 Internal waves around a body moving in a compressible density-stratified fluid. *J. Fluid Mech.* **70** (4), 673–688.

PHAM, H. T., SARKAR, S. & BRUCKER, K. A. 2009 Dynamics of a stratified shear layer above a region of uniform stratification. *J. Fluid Mech.* **630**, 191–223.

PLOUGONVEN, R. & ZEITLIN, V. 2002 Internal gravity wave emission from a pancake vortex: an example of wave–vortex interaction in strongly stratified flows. *Phys. Fluids* **14**, 1259.

RILEY, J. J. & DE BRUYN KOPS, S. M. 2003 Dynamics of turbulence strongly influenced by buoyancy. *Phys. Fluids* **15**, 2047–2059.

RILEY, J. J. & LINDBORG, E. 2008 Stratified turbulence: a possible interpretation of some geophysical turbulence measurements. *J. Atmos. Sci.* **65** (7), 2416–2424.

RILEY, J. J. & METCALFE, R. W. 1987 Direct numerical simulations of turbulent patches in stably-stratified fluids. In *Stratified Flows I. Proceedings 3rd International Symp. on Stratified Flows*, California Institute of Technology, Pasadena.

RILEY, J. J., METCALF, R. W. & WEISSMAN, M. A. 1981 Direct numerical simulations of turbulence in homogeneously stratified fluids. In *Non-linear Properties of Internal Waves*, pp. 79–112. AIP.

ROBEY, H. F. 1997 The generation of internal waves by a towed sphere and its wake in a thermocline. *Phys. Fluids* **9**, 3353.

SMYTH, W. D. 1999 Dissipation-range geometry and scalar spectra in sheared stratified turbulence. *J. Fluid Mech.* **401**, 209–242.

SMYTH, W. D. & MOUM, J. N. 2000 Length scales of turbulence in stably stratified mixing layers. *Phys. Fluids* **12**, 1327.

SPEDDING, G. R. 1997 The evolution of initially turbulent bluff-body wakes at high internal Froude number. *J. Fluid Mech.* **337**, 283–301.

SPEDDING, G. R. 2002 Vertical structure in stratified wakes with high initial Froude number. *J. Fluid Mech.* **454**, 71–112.

SPEDDING, G. R., BROWAND, F. K., BELL, R. & CHEN, J. 2000 Internal waves from intermediate, or late-wake vortices. In *Stratified Flows I – Fifth International Symposium* (ed. R. Pieters, N. Yonemitsu & G.A. Lawrence), vol. 1, pp. 113–118. University of British Columbia, Vancouver.

SPEDDING, G. R., BROWAND, F. K. & FINCHAM, A. M. 1996 Turbulence, similarity scaling and vortex geometry in the wake of a towed sphere in a stably stratified fluid. *J. Fluid Mech.* **314**, 53–103.

SPEDDING, G. R., BROWAND, F. K., HUANG, N. E. & LONG, S. R. 1993 A 2-D complex wavelet analysis of an unsteady wind-generated surface wave field. *Dyn. Atmos. Oceans* **20** (1–2), 55–77.

DE STATLER, M. B., SARKAR, S. & BRUCKER, K. A. 2010 Effect of the Prandtl number on a stratified turbulent wake. *Phys. Fluids* **22**, 095102.

SUTHERLAND, B. R. 2001 Finite-amplitude internal wavepacket dispersion and breaking. *J. Fluid Mech.* **429**, 343–380.

SUTHERLAND, B. R. 2010 *Internal Gravity Waves*. Cambridge University Press.

SUTHERLAND, B. R., FLYNN, M. R. & DOHAN, K. 2004 Internal wave excitation from a collapsing mixed region. *Deep-Sea Res.* II **51**, 2889–2904.

SUTHERLAND, B. R. & LINDEN, P. F. 1998 Internal wave excitation from stratified flow over a thin barrier. *J. Fluid Mech.* **377**, 223–252.

TAYLOR, J. R. & SARKAR, S. 2007 Internal gravity waves generated by a turbulent bottom Ekman layer. *J. Fluid Mech.* **590**, 331–354.

TAYLOR, J. R. & SARKAR, S. 2008 Stratification effects in a bottom Ekman layer. *J. Phys. Oceanogr.* **38** (11), 2535–2555.

THORPE, S. A. 2005 *The Turbulent Ocean*. Cambridge University Press.

TOWNSEND, A. A. 1965 Excitation of internal waves by a turbulent boundary layer. *J. Fluid Mech.* **22** (2), 241–252.

TOWNSEND, A. A. 1968 Excitation of internal waves in a stably-stratified atmosphere with considerable wind-shear. *J. Fluid Mech.* **32** (1), 145–171.

TRAUTH, M. H. 2010 *MATLAB® Recipes for Earth Sciences*. Springer.

VOISIN, B. 1991 Internal wave generation in uniformly stratified fluids. Part 1. Green's function and point sources. *J. Fluid Mech.* **231**, 439–480.

VOISIN, B. 1994 Internal wave generation in uniformly stratified fluids. Part 2. Moving point sources. *J. Fluid Mech.* **261**, 333–374.

WIJESEKERA, H. W. & DILLON, T. M. 1991 Internal waves and mixing in the upper equatorial Pacific Ocean. *J. Geophys. Res.* **96** (C4), 7115–7125.

WU, J. 1969 Mixed region collapse with internal wave generation in a density-stratified medium. *J. Fluid Mech.* **35** (3), 531–544.

ZAVOL'SKII, N. A. & ZAITSEV, A. A. 1984 Development of internal waves generated by a concentrated pulse source in an infinite uniformly stratified fluid. *J. Appl. Mech. Tech. Phys.* **25** (6), 862–867.